PROCEEDINGS A

rspa.royalsocietypublishing.org

Review

Cite this article: Ferrari A. 2017 Fluid dynamics of acoustic and hydrodynamic cavitation in hydraulic power systems. *Proc. R. Soc. A* **473**: 20160345.
http://dx.doi.org/10.1098/rspa.2016.0345

Received: 22 May 2016
Accepted: 20 December 2016

Subject Areas:
power and energy systems, mechanical engineering, mathematical modelling

Keywords:
acoustic cavitation, hydrodynamic cavitation, sound speed, nozzle discharge coefficient, Rayleigh–Plesset equation, barotropic and baroclinic models

Author for correspondence:
A. Ferrari
e-mail: alessandro.ferrari@polito.it

Fluid dynamics of acoustic and hydrodynamic cavitation in hydraulic power systems

A. Ferrari

Energy Department, Politecnico di Torino, Corso Duca degli Abruzzi 24, 10129 Torino, Italy

AF, 0000-0001-6980-2325

Cavitation is the transition from a liquid to a vapour phase, due to a drop in pressure to the level of the vapour tension of the fluid. Two kinds of cavitation have been reviewed here: acoustic cavitation and hydrodynamic cavitation. As acoustic cavitation in engineering systems is related to the propagation of waves through a region subjected to liquid vaporization, the available expressions of the sound speed are discussed. One of the main effects of hydrodynamic cavitation in the nozzles and orifices of hydraulic power systems is a reduction in flow permeability. Different discharge coefficient formulae are analysed in this paper: the Reynolds number and the cavitation number result to be the key fluid dynamical parameters for liquid and cavitating flows, respectively. The latest advances in the characterization of different cavitation regimes in a nozzle, as the cavitation number reduces, are presented. The physical cause of choked flows is explained, and an analogy between cavitation and supersonic aerodynamic flows is proposed. The main approaches to cavitation modelling in hydraulic power systems are also reviewed: these are divided into homogeneous-mixture and two-phase models. The homogeneous-mixture models are further subdivided into barotropic and baroclinic models. The advantages and disadvantages of an implementation of the complete Rayleigh–Plesset equation are examined.

1. Introduction

The term ‘cavitation’ generally describes the process of growth and collapse of the vapour phase in a liquid, when the local liquid pressure drops below the saturation pressure at a given temperature. Cavitation is responsible for issues such as erosion [1,2], noise and vibration

THE ROYAL SOCIETY PUBLISHING

[3,4], which can lead to the malfunctioning of various turbo-machines [5] and positive displacement machines. In general, the occurrence of cavitation has a negative effect on the proper functioning of a hydraulic system. However, in some particular cases, it can also have a positive effect, as it can lead to a drag reduction, as in the case of submarine vehicles [6], or to a better liquid atomization, as in the case of fuel injector holes [7]. It is important to be able to understand the physics behind the two-phase flow phenomenon in order to reduce the negative effect, or to increase its positive influence. In this sense, obtaining detailed knowledge on the basic theoretical aspects of cavitation, and studying cavitation dynamics in simple geometries, such as pipes and nozzles, is one way of achieving this goal [8].

Cavitation inception is the process by which bubbles develop within a liquid when the local tension $(p_v - p) \geq 0$ (table 1) exceeds the tensile strength of the liquid [9]. After this limit has been exceeded, a general explosive growth of the gaseous nuclei can be observed. The value of the tensile strength of a liquid depends on the presence of weak spots in the liquid, which provide the nuclei for the development of the phase transition process. Because the mass of the vaporized phase is usually much smaller than the mass of the liquid phase, the amount of heat consumed locally to vaporize tiny amounts of liquid can be neglected in a macroscopic analysis. Hence, the global evolution of the cavitating flow can be regarded as an isothermal process, although the heat of vaporization of the liquid is not negligible. The macroscopic effects of thermodynamic evolution on cavitation have been analysed in [10]: some differences appear in the intensity of the phenomena, such as the maximum void fraction or the minimum pressure values, but the primary events and the main dynamics of the cavitation zone are not affected to any great extent when different thermodynamic laws are adopted.

Cavitation desinence refers to the process by which the vapour phase vanishes from the liquid, as a result of a pressure increase in the liquid flow that surrounds the bubbles. During the final collapse stage of the bubbles, the temperature and pressure can become extremely high inside the bubbles, due to the inertia and compressibility of the gas-vapour bubble content. These high temperatures, and the presence of intense and high-frequency pressure waves, which are triggered by the peak pressure values that are reached after the bubble has collapsed, lead to the possible production of light emission (sonoluminiscence) and to erosive wear of the surfaces of the hydraulic systems. Erosion occurs because the pressure waves remove the layer of oxides that had previously formed on the hydraulic system walls, and the air content in the liquid can therefore oxidize a new layer on these walls, which progressively become thinner.

A possible classification of vaporous cavitation can be made on the basis of the reasons for the pressure reduction. Acoustic cavitation is induced by the presence of pressure waves that propagate through the liquid region [11,12]. This often takes place in hydraulic power systems, such as high-pressure diesel injection apparatus, continuously variable transmission systems, anti-lock braking systems and traction control systems. In such cases, acoustic cavitation can be accurately studied by means of refined, unsteady, one-dimensional models [13–16].

Hydrodynamic cavitation occurs when the reduction in pressure to the vapour tension level is caused by the hydrodynamic motion of the fluid, the features of which in turn depend on the geometrical layout of the flow passages [17,18]. The liquid pressure can decrease locally, below the vapour tension level, according to Bernoulli's equation, as a result of augmenting the gravitational energy, or the kinetic energy, of a fluid. An increase in gravitational energy can occur in a piping system, when the pipe elevation increases locally; an increase in kinetic energy can result from an abrupt reduction in the cross-section of the flow passages, such as in diesel injector holes [17,19,20], but also because of a particular design of the walls that delimitate the flow, for example, around the rotor blades of dynamic pumps or in marine propellers [21]. Decreases in the local pressure caused by concentrated losses at the inlet of positive displacement and vane pumps, particularly when special valves are installed at the pump inlet to control the flow rate, can also result in cavitation.

It is necessary to use two-dimensional or three-dimensional models to conduct an accurate simulation of hydrodynamic cavitation, because of its local nature. Unlike acoustic cavitation, which is initiated by unsteady pressure waves that travel throughout the liquid, hydrodynamic

Table 1. Nomenclature.

a	speed of sound of the fluid
b	parameter in the expression of the nucleus-size spectral distribution function
A	cross-section of the nozzle; tuneable coefficient in the discharge coefficient model
B, C	tuneable coefficients in the discharge coefficient model; parameters in Tait's equation
B^*, C^*	parameters in Tamman's equation
C_c	contraction coefficient
C_d	discharge coefficient
c_p	specific heat at constant pressure
C_v	velocity coefficient
CN	cavitation number
d	diameter of the cylindrical nozzle
E_T	modulus of elasticity of the fluid
K_{loss}	concentrated loss term
L	length of the nozzle; length of the pipe connecting the pump to the injector
L_{cav}	cavitation zone length
L_{sep}	separation zone length
m	exponent in the expression of the nucleus-size spectral distribution function
$\dot{m}$	actual mass flow rate
$\dot{m}_{id}$	ideal mass flow rate
Ma	Mach number
n	number of bubbles per unit volume of liquid phase
$N(R)$	nucleus-size spectral distribution function
p	pressure
q	vaporization heat of the fluid
Q	volumetric flow rate
R	bubble radius
$\dot{R}$	time derivative of the bubble radius
$\ddot{R}$	second time derivative of the bubble radius
r_{in}	fillet radius at the inlet edge of the nozzle
R_v	molecular constant of the vapour
Re	Reynolds number
s	liquid surface tension
t	time
T	temperature
u	velocity of the fluid in the pipe of the fuel injection system
$\bar{u}$	section averaged velocity of the stream (nozzle)
U	characteristic velocity scale for the considered problem

(*Continued*.)

Table 1. (*Continued*.)

v	specific volume
V	volume
x	axial coordinate along the pipe
α	void fraction
β	Coriolis coefficient of the stream; thermal expansivity of the fluid
Γ	vapour source term in the mass conservation equation
δ	laminar flow coefficient
Δp	pressure difference across the nozzle
λ	Moody factor
η	dynamical viscosity of the fluid
θ	pumpshaft angle
μ	mass fraction
ν	kinematic viscosity of the fluid
ξ	average radius in the expression of the nucleus-size spectral distribution function
Π	Euler number for cavitation
ρ	density of the fluid
Σ	standard deviation in the expression of the nucleus-size spectral distribution function
τ_{cond}	time constant for liquid reconversion
τ_{ev}	time constant for vapour formation
χ	nozzle shape coefficient
ψ	fitting parameter in the expression of the nucleus-size spectral distribution function
subscript	
B	inside the bubble
c	referring to the vena contracta
cr	referring to critical conditions (choked flow); referring to the Blake radius
g	undissolved gas within the bubble
l	liquid phase
max	maximum value
min	minimum value
sat	saturation value
start	at cavitation inception
v	vapour phase
0	initial conditions
1	referring to the upstream environment of the nozzle
2	referring to the downstream environment of the nozzle
∞	at a great distance from the bubble; asymptotic value

cavitation can also take place in steady-state flows. Some typical hydrodynamic cavitation problems of engineering relevance in hydraulic power applications are those related to straight or conical nozzles and to orifices: in these cases, the main objective of an analysis is to obtain an accurate calculation of the nozzle discharge coefficient.

Experimental methods generally provide a reliable basis to analyse hydrodynamic cavitation flows, but studies on cavitation in engineering components of reduced size, such as injector holes, orifices and miniaturized hydraulic valves, are difficult, because of the special equipment and techniques necessary to measure and visualize the flow. In these cases, hydrodynamic cavitation can be studied using the hydrodynamic similarity theory [22,23]. Different nozzle prototypes have been realized with optical materials, such as quartz and methacrylate, which allow the velocity components inside the nozzles to be visualized [24]: some studies have been performed with planar nozzles, in order to be able to observe cavitation more easily [25–28], while others have been conducted with large-scale cylindrical nozzles [23,29–32], in order to facilitate the visualization of the phenomena. Observations in the laboratory can be extrapolated to natural-scale flows [33–36], through the use of a scale model and different fuels, and the obtained results can then be integrated with data from a few experimental studies on cavitation in real-size orifices [35,37,38].

An alternative methodology to the experimental investigation of hydrodynamic cavitation is represented by its numerical computation. Models based on Navier–Stokes equations and standard turbulence models have become very attractive for the prediction of cavitating flow fields of arbitrary scales, because they are able to cope with the evaluation of secondary scale effects. Furthermore, the governing partial differential equations of the model can be arranged in dimensionless form, in order to exploit the advantages of hydrodynamic similarity. However, two-dimensional and three-dimensional computation approaches to cavitation are not yet at a fully mature stage, as the single-phase calculations of acoustic cavitation instead are, and they still need improvements and practice in order to increase confidence in the results [39].

2. Application of hydrodynamic similarity to cavitating flows in straight nozzles

The conditions necessary to allow the experimental observations of a cavitation flow in one scale to be transferred to another scale, according to the theory of hydrodynamic similarity [33,34,40,41], are the geometrical similarity of the flows and the identification of some dimensionless groups, which are defined with some macroscopic quantities. Thermal aspects, any local features of the problem, including details on the nozzle geometry (for example, conicity of the nozzle and roundness at its entry), and the fluid dynamic characterization of two-phase structures can initially be disregarded in an investigation that is focused on the macroscopic effects of cavitation. The nozzle discharge coefficient, C_d, can be expressed as a function of the following dimensionless numbers in a turbulent field [42,43]:

$$\begin{cases} C_d = C_d\left(Re, \dfrac{L}{d}\right) & \text{for liquid flows,} \\ C_d = C_d\left(\mathrm{CN}, \dfrac{L}{d}\right) & \text{for cavitating flows.} \end{cases} \tag{2.1}$$

Parameter $Re = \rho_l U d/\eta_l$ is the Reynolds number of the nozzle, where U is a velocity scale of the flow, d is the internal diameter of the nozzle, and ρ_l and η_l are the density and dynamical viscosity of the liquid fluid; $\mathrm{CN} = (p_1 - p_v)/(p_1 - p_2)$ is the cavitation number, where p_v is the vapour tension of the flow, p_1 and p_2 are the upstream and downstream pressures of the nozzle, and L/d is the aspect ratio of the cylindrical nozzle, where L is its length. The L/d ratio becomes relevant as a dimensionless parameter for the evaluation of C_d in relatively long nozzles ($L/d > 10$): the main influence of L/d on the discharge coefficient is generally ascribed to frictional losses, and to boundary layer development in the liquid flow region downstream of the flow reattachment point [44]. The effect of L/d on cavitation inception and development is only marginal, because these phenomena are local; the complete cavitation sub-regimes, such as supercavitation and hydraulic flip, can instead be affected more appreciably by the L/d ratio, because they involve the whole nozzle. When the focus is not on supercavitation and hydraulic flip, it is possible to consider $C_d \approx C_d(\mathrm{CN})$ for cavitating flows [24,43]. The functional dependencies stated in equation (2.1) can be deduced, by means of the Buckingham theorem, after reasonable simplifications

of the problem, but experimental or numerical analyses are needed to determine the exact analytical laws. Experimental studies [35] have confirmed that the steady-state macroscopic features of hydro-dynamic cavitation are similar for all real-size (with a diameter smaller than 1 mm) and large-scale nozzles, and that the cavitation number is the most suitable criterion for data comparisons [43,45].

On the other hand, experiments have also shown that real flows do not always obey the classical scaling theory, and discrepancies can occur between cavitation flows under natural and large-scale conditions [46]. The reasons for these discrepancies are: secondary-scale effects related to micro-geometrical differences, which are caused by wall roughness [28] and by details of the nozzle geometry, such as roundness at the nozzle inlet [47,48] and nozzle conicity, or the K-factor of the hole [48,49]; local-flow motion, which is related to the influence of the viscous stresses on the tensile strength of a liquid [50,51] (the classic definition of cavitation inception is based on observations of liquid rupturing under static or quasi-static conditions [9], that is, when the static pressure in the liquid phase is much higher than the viscous stresses caused by the flow, but, if this is not the case, the tensile strength can be affected by the viscous stresses) and to the turbulent and transient nature of hydrodynamic cavitation [52–55]; liquid quality, which is characterized by means of the radius and density of the undissolved-gas microbubbles in the fluid as well as by the concentration of dissolved gas in the liquid phase [9,56]. In other words, the scale effects associated with the micro-geometry of the system, the local flow phenomena and the liquid quality should have a negligible effect on the considered tests in order to make equation (2.1) valid. As long as this condition is verified, only those discrepancies concerning the details of the cavitation description will occur if real- and large-scale nozzles are compared; otherwise micro-geometrical, local-flow and liquid-quality-scale effects should be characterized and modelled in an appropriate manner.

3. Different hydrodynamic cavitation regimes in nozzles

As can be inferred from figure 1, cavitation takes place in the low-pressure region that forms at the nozzle entry [57], and in the zone around the section at which the jet flow area is at the minimum (this section of area A_c is referred to as the vena contracta). The figure shows that the separation zone (with length L_{sep}) and the cavitation zone (with length L_{cav}) do not generally coincide: the separation zone occurs downstream of a sudden change in the flow path geometry, and this separation can exist with or without cavitation. After the main stream has reattached to the wall, the pressure reduction in the subsequent piece of the straight nozzle is due to wall friction, and a boundary layer starts growing from the reattachment point up to the nozzle exit [43]. The value of the cavitation number, i.e. $\mathrm{CN} = (p_1 - p_v)/(p_1 - p_2)$, determines the extent of the region that is filled with vapour inside the nozzle.

Figure 2 schematically illustrates the influence of p_2 on the length of the cavitation region for a one-dimensional de Laval nozzle (x is the axial coordinate along the nozzle). As p_2 reduces, cavitation occurs in correspondence with the nozzle throat (cavitation develops for a p_2 value that corresponds to B''). If p_2 is diminished even further, the cavitation region, in which the pressure is equal to p_v, progressively extends towards the nozzle exit. The cavitation region in figure 2 starts at point B' and extends to point D', if the p_2 value corresponds to D'', but it can also extend to point E', if p_2 reduces to the value that corresponds to E''. The pressure recovery from p_v up to p_2 occurs in the divergent part of the de Laval nozzle, downstream of the cavitation region.

A classification of the cavitation regimes has been made in figure 3, where L_{cav} is the length of the cavitation region (cf. figure 1), as CN is progressively reduced [58]

— incipient cavitation occurs as soon as cavitation starts at the nozzle entrance;
— the developed cavitation regime is constituted by an early sub-cavitation stage, in which the vapour tends to fill the separation region of axial extension L_{sep} (cf. figure 1) as CN diminishes (CN has little effect on L_{cav} in this sub-regime), and by a further transitional

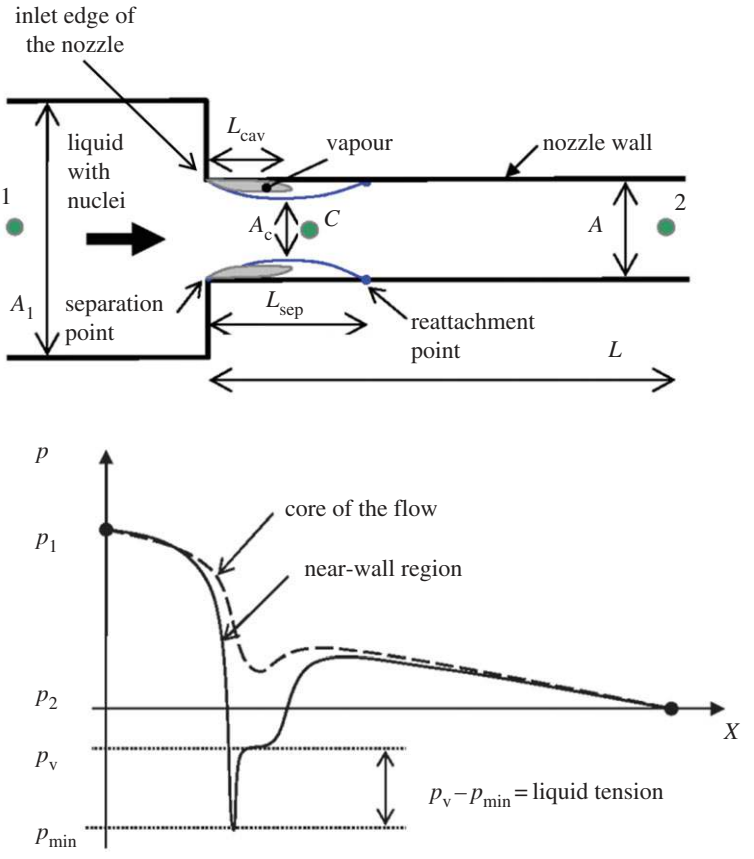

Figure 1. Straight nozzle layout and pressure evolution. (Online version in colour.)

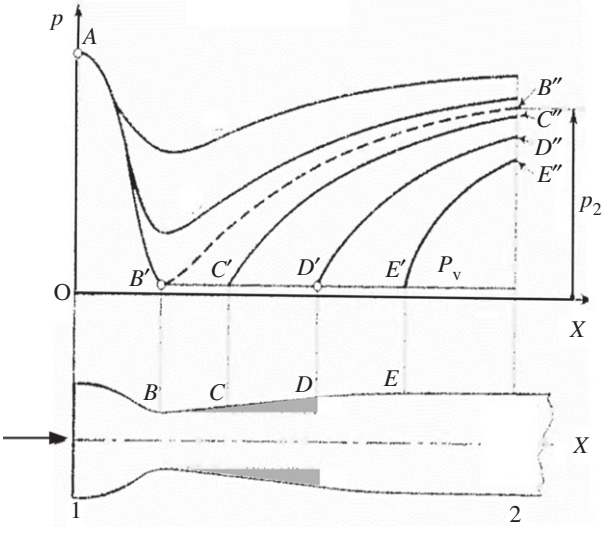

Figure 2. Cavitation evolution with respect to p_2.

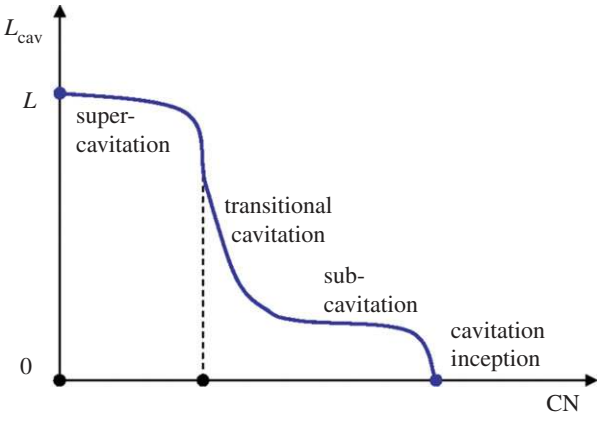

Figure 3. Different cavitation regimes. (Online version in colour.)

cavitation sub-regime, in which L_{cav} extends significantly downstream from the vena contracta as CN diminishes, and

— supercavitation occurs when the cavity length develops up to or close to the nozzle exit ($L_{cav} \rightarrow L$): the liquid core in this regime is surrounded by a vapour cloud, which can eventually fill the whole nozzle and make the liquid core disappear. Supercavitation can also be defined as a regime with a clear vapour–liquid separation layer.

Observations on small-scale nozzles have revealed the presence of bubbly flow and bubble foam patterns in the incipient, sub-cavitation and early transitional cavitation stages, while sheet-type cavitation, with the presence of long strips and vapour films, has been observed well into the transitional cavitation sub-regime, and in the supercavitation regime [51]. In other words, the features of the vapour structures at cavitation inception are almost the same regardless of the nozzle geometry, and the development and early evolution of these structures is not affected by this geometry. However, the shape of the cavitation structures, during the deep transitional regime and the supercavitation regime, depends on the nozzle geometry to a significant extent.

The high-speed photography of supercavitation flows [58] has revealed their unsteady and unstable nature. As soon as the flow starts to enter the supercavitation regime, a rapid collapse of the cavitation pockets can occur between the liquid core and the walls, according to a re-entrant jet mechanism [59]. It is believed that the re-entrant jet is created by the expansion of the flow in the closure region behind the cavity; this flow impinges on the wall and establishes a local stagnation point. On the upstream side of this stagnation point, conservation of the momentum forces the liquid to flow beneath the fixed cavity. The jet progresses towards the nozzle inlet and, even though no liquid layer can completely separate the vapour phase from the walls [54], it pinches off the fixed cavity and a vapour cloud is formed [54]. As the cloud is shed, the remaining cavity at the nozzle inlet again begins to grow. The separated cloud that is convected downstream eventually collapses in the relatively high-pressure region behind the flow-reattachment point. The motion of the re-entrant liquid jet is central to the periodic shedding of the cavitation cloud, but the mechanism that drives the phenomenon is still not fully known [54]. It has been observed [60] that the re-entrant jet is dominant during the earlier stages of the instability, whereas a propagating shock wave appears during the later stages for the intensive cloud-shedding phase [61].

It is also of interest, from the supercavitation instability point of view, to recall that, once the vapour fixed cavity reaches about 25–35% of nozzle length L [58,62], the point of cavity reattachment can move instantly at the nozzle exit, and can thus suddenly enter the supercavitation regime. This is illustrated in figure 3, where the L_{cav} versus CN curve exhibits a vertical inflection point between transitional cavitation and supercavitation.

The cavitation zone at the lowest CN values can exceed the nozzle ($L > L_{cav}$), and a jet cavitation occurs if the nozzle is submerged in a liquid [58] (this is not shown in figure 1, where L_{cav} is saturated at L). On the other hand, when the outflow is into a gas, experiments [23,63] have shown that the liquid flow is unable to reattach to the nozzle walls at the lowest CN values. Cavitation disappears, and a jet that consists entirely of liquid (a glass-like flow [63]) becomes completely detached from the nozzle walls: this regime is referred to as hydraulic flip [18,64]. The latter circumstance causes minimum values of the discharge coefficient [63], and thus reduces the liquid flow penetration in the downstream environment, which in turn results in altered spray characteristics. Nevertheless, hydraulic flip also determines a sudden reduction in friction losses, because there is no contact between the liquid flow and the nozzle walls.

As the L/d ratio increases, slightly lower CN values are generally required to induce cavitation inception [65,66], and lower CN values are required to enter the supercavitation regime [67], because flow reattachment is more likely to occur. Furthermore, no hydraulic flip occurs for $L/d \geq 8$, whereas it does occur for $L/d = 4$ in the injection holes that have recently been analysed by Zhong *et al*. [23]. Rounded inlet corners of straight nozzles also affect the recirculation flow that forms at the nozzle throat: L_{sep} reduces and transition to hydraulic flip is more unlikely [67].

4. Nozzle discharge coefficient models

The nozzle discharge coefficient represents the hydraulic resistance of a nozzle to the flow passage. It can be defined as

$$C_d = \frac{\dot{m}}{\dot{m}_{id}}, \tag{4.1}$$

where $\dot{m}$ is the actual mass flow rate through the nozzle, $\dot{m}_{id} = \frac{A}{\sqrt{\beta}}\sqrt{2\rho_l(p_1 - p_2) + \beta\rho_l^2\,\bar{u}_1^2}$ is the ideal mass flow rate, according to the Bernoulli equation for a stream, $A = \pi\, d^2/4$ is the cross-section of the straight nozzle (figure 1), $\bar{u}_1$ is the mass average velocity of the flow in the upstream reservoir of the nozzle and $\beta = \int_A u^2 \mathrm{d}\dot{m}/(\bar{u}^2\dot{m})$ is the Coriolis coefficient of the stream (β is usually in the 1.05–1.2 range). Different expressions of C_d are available in the literature: an important aspect of their formulation concerns the presence or absence of cavitation in the nozzle.

(a) Cavitating flow

The combined application of the mass conservation equation and of the generalized Bernoulli equation for an incompressible flow (with $\beta \neq 1$), between sections 1 and C (figure 1), taking into account the volumetric flow-rate conservation equation between sections C and 2, leads to the following theoretical expression for C_d [51]:

$$C_d = \frac{C_v C_c (CN)^{1/2}}{\sqrt{[1 + C_c^2 (A/A_1)^2 (C_v^2 CN - 1)]}}, \tag{4.2}$$

where A_1 is the cross-section in the upstream reservoir (figure 1). Term C_c is the contraction coefficient, which is defined as

$$C_c = \frac{A_c}{A}, \tag{4.3}$$

where A_c is the vena contracta (figure 1). Furthermore, the term $C_v < 1$ is the friction coefficient, which accounts for viscous losses that occur from the upstream section of the nozzle up to the vena contracta (C_v can be defined as the ratio of the actual velocity at the vena contracta to the corresponding ideal velocity in the absence of friction) [68]. Neglecting the velocity in section 1 in figure 1 ($\bar{u}_1 \approx 0$) implies that the A/A_1 ratio tends to zero ($A_1 \to \infty$), and equation (4.2) reduces

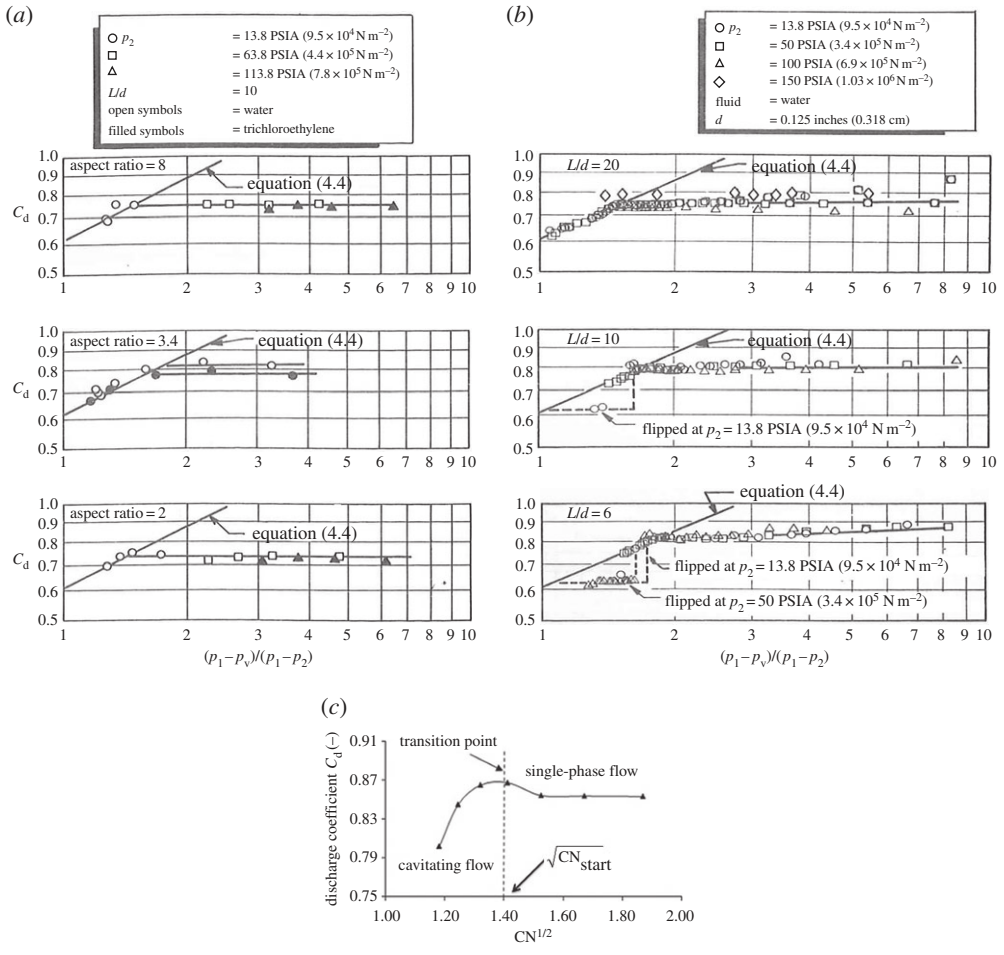

Figure 4. Dependence of C_d on CN. (*a*) Rectangular cross-section nozzle [43]. (*b*) Circular cross-section nozzle [43]. (*c*) Cavitation inception and development.

to the following simplified correlation:

$$C_d \approx C_v C_c \sqrt{CN}. \tag{4.4}$$

As already mentioned, CN represents the main parameter necessary for the characterization of C_d during cavitation [23]. CN is sometimes replaced by the following dimensionless number, which is a special form of the Euler number [53,69]:

$$\Pi = \frac{p_2 - p_v}{\rho_l U^2/2}, \tag{4.5}$$

where $U = \sqrt{2(p_1 - p_2)/\rho_l}$. Euler's cavitation number Π can easily be expressed in terms of CN, according to relation $CN = 1 + \Pi$.

Figure 4 emphasizes the relationship between C_d and CN: figure 4*a* refers to a nozzle with a rectangular cross-section (the aspect ratio in this case is the ratio of the longer size to the lower size of the rectangular cross-section), whereas figure 4*b* refers to a nozzle with a circular cross-section. The data plotted in figure 4*a*,*b*, which refer to inside the cavitation region, that is, where C_d depends significantly on CN, have been interpolated using equation (4.4).

The dependence of C_d on CN is not significant in the liquid flow regime, where the mass flow rate depends almost linearly on the square root of the pressure drop across the nozzle, i.e. on $\sqrt{p_1 - p_2}$.

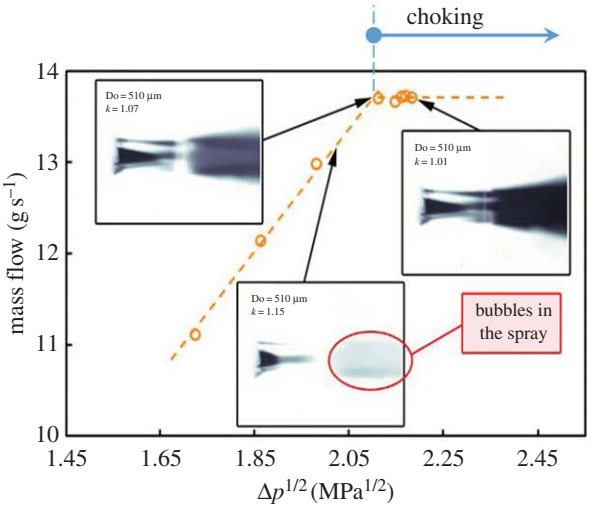

Figure 5. Mass flow rate, cavitation and choking conditions for diesel oil (p_1 is constant and p_2 changes) [24]. (Online version in colour.)

A slight increase in C_d can be observed in the initial cavitation stage in figure 4*c*, in line with the results of other visualization experiments [65]. This particular phenomenon may be explained by considering that the very small amount of bubbles, located at the inlet corner of the nozzle, smooth the internal flow, and thus improve the discharge coefficient [65]. A criterion that has been proposed to detect cavitation inception, which is related to the appearance of the first bubbles [24], pertains to the identification of CN_{start} (this is the CN value that corresponds to cavitation inception) through the use of the value of CN that corresponds to the maximum of C_d [62].

The discharge coefficient diminishes significantly as CN reduces, once the vapour region has already become extended, that is, as soon as flow choking due to cavitation occurs, as can also be inferred from figure 5 ($\Delta p = p_1 - p_2$).

The small oscillations, with respect to $\Delta p^{1/2}$, which affect the choked flow rate in figure 5 (close to $\Delta p^{1/2} \approx 2.1$), are the result of unsteady processes and instability phenomena inside the nozzle during the supercavitation regime.

The greyscale images that are included in figure 5 refer to internal flow visualizations of the nozzle measured by means of an optical system [24]. The cavitation zones are dark, and the darkness intensity increases as the cavitation intensity increases. It can be observed that bubbles are already present in the spray within the nozzle before choking takes place. Furthermore, the choked flow occurs in correspondence to a $\Delta p^{1/2}$ value that is close to the one for which cavitation extends up to the orifice exit.

(b) Liquid flow and dependence of C_d on *Re*

The discharge coefficient of a straight nozzle for cavitation-free flows, for which pressure p_c is higher than p_v at the vena contracta, is mainly a function of the Reynolds number of the nozzle, that is, $Re = d\sqrt{2\rho_l(p_1 - p_2)}/\eta_l$.

An empirical correlation that is often used to describe both the effects of *Re* and the aspect ratio on the discharge coefficient of the cylindrical nozzle is [70]

$$C_d = \left(1.23 + \frac{58 \cdot L/d}{Re}\right)^{-1}, \tag{4.6}$$

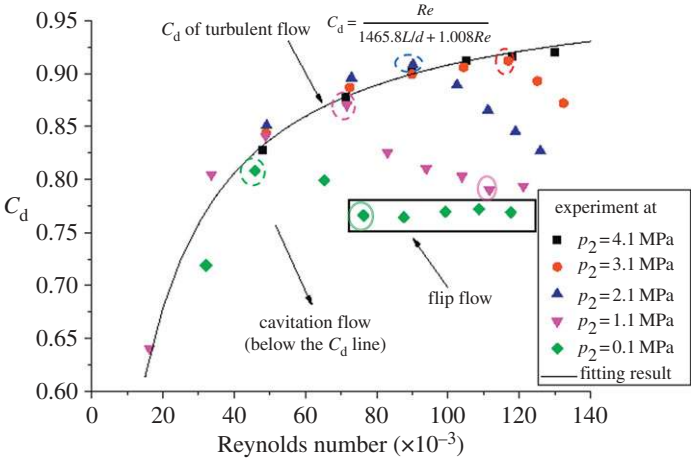

Figure 6. C_d versus *Re* [71]. (Online version in colour.)

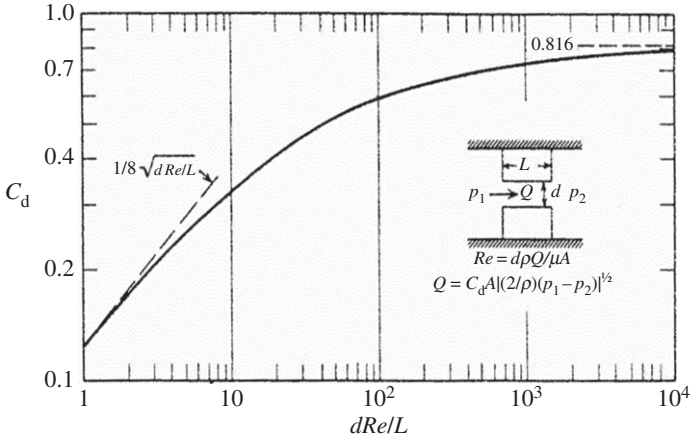

Figure 7. Influence of L/d on the C_d versus *Re* curve for oil [68].

which is valid for $Re < 1.5 \times 10^5$ and in the $2 < L/d < 5$ range. Another robust interpolating expression, which expresses C_d as a function of *Re* and which is valid for $Re < 10^5$, is given by [24]

$$C_d = A \tanh\left(\frac{Re + C}{B}\right), \tag{4.7}$$

where A, B and C are tunable coefficients and are constant for a given nozzle.

Figure 6 refers to water and a cylindrical nozzle with fixed L and d values. The tests have been conducted by varying the upstream pressure p_1 for different levels of p_2, and the solid line interpolates the experimental data in the liquid field, according to the formula that is reported in the graph. Furthermore, figure 7 plots the experimental data of C_d as a function of $Re(L/d)^{-1}$ for mineral oil; the quantity reported at the abscissa is in line with the analytical dependence of the discharge coefficient in the C_d expression in figure 6, and with equation (4.6). However, there are formulae in which the analytical dependence of C_d on *Re* can be different from that of C_d on d/L.

Figure 6 also shows the experimental results in the cavitation and hydraulic-flip regimes. In general, C_d increases as *Re* increases for a liquid flow, and tends to an asymptotic value, then abruptly decreases as *Re* increases in the cavitation regime, due to the presence of cavitation choking, and finally remains constant because of hydraulic flip [71]. The hydraulic-flip behaviour in figure 6 is consistent with what can be observed in figure 4*b*. The critical Reynolds number (Re_{cr}) at which the sudden reduction in C_d takes place, because of choking, is always within the

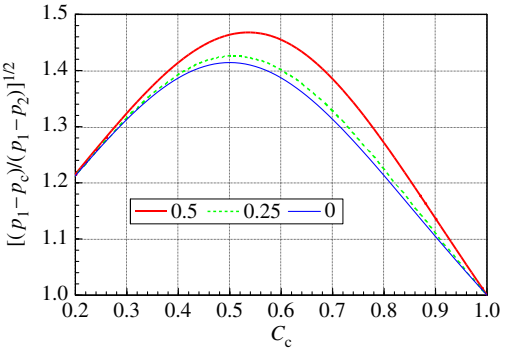

Figure 8. Square root of $(1+\chi)^{1/2}$ as a function of C_c for different A_2/A_1 ratios. (Online version in colour.)

turbulent field, and can be determined for the different p_2 values by considering the first inflection point along the C_d versus Re curve (symbol contoured with a dashed circle for each $p_2 \leq 3.1$ MPa). Hydraulic flip takes place at the second inflection point along this curve [71] (symbol contoured with a solid circle for $p_2 \leq 1.1$ MPa). As can be inferred, Re_{cr} depends on p_2, and increases as p_2 grows, because the tendency to cavitation is counteracted by any augmentation in p_2; Re_{cr} has also been shown to depend on the type of liquid (water, oil, etc.) [24].

An alternative method to the application of empirical expressions, such as equations (4.6) and (4.7), consists in developing theoretical formulae for C_d for liquid flows. By writing Bernoulli's equation for a liquid stream, from section 1 to section 2 (figure 1), it is possible to obtain an estimation of the discharge coefficient for a straight nozzle [62,63]:

$$\bar{u}_2 \approx \frac{1/\sqrt{\beta}}{\sqrt{1+\bar{\lambda}_2\, L/d + K_{loss}}}\sqrt{2(p_1-p_2)/\rho_l + \beta\,\bar{u}_1^2} \Rightarrow C_d \approx \frac{1}{\sqrt{1+\bar{\lambda}_2\, L/d + K_{loss}}}, \tag{4.8}$$

where $\bar{\lambda}_2$ is the Moody factor, evaluated at section 2 in figure 1 as a function of $\overline{Re}_2 = \rho_l \bar{u}_2 d/\eta_l$, and K_{loss} is an empirical term that describes the dependence of the concentrated loss, due to a sudden contraction, on the diameter ratio; as an example, $K_{loss} = 1/2(1-d/d_1)$ for oil [68].

It is also possible to adapt the theoretical expression of C_d given by equation (4.4) to cavitation-free flows by substituting p_v with p_c ($p_c > p_v$), from which one obtains

$$C_d \approx C_c C_v \sqrt{\frac{p_1-p_c}{p_1-p_2}}. \tag{4.9}$$

The pressure recovery, downstream from vena contracta region C up to section 2 in figure 1, can be estimated by applying the momentum balance equation to the stream. If friction losses are neglected and $\beta = 1$, one obtains [72]

$$\chi = \frac{p_2-p_c}{p_1-p_2} = \left[\frac{C_c^{-2} - (A/A_1)^2}{C_c^{-2} - (A/A_1)^2 - 2(C_c^{-1}-1)} - 1\right], \tag{4.10}$$

where χ is referred to as the nozzle shape coefficient. On the basis of equation (4.10), figure 8 plots the $(1+\chi)^{1/2} = \sqrt{(p_1-p_c)/(p_1-p_2)}$ term, which appears in equation (4.9), as a function of C_c, for the different A/A_1 values that are quoted in the graph. As can be inferred, the square root term is constant for a given nozzle, and is significantly higher than 1 over the $0.2 \leq C_c < 0.8$ range. This means that there has been a significant pressure recovery from C up to 2.

The subsequent expression can be obtained, for the $A/A_1 \to 0$ case, from equations (4.9) and (4.10)

$$C_d = \frac{C_v}{\sqrt{C_c^{-2} - 2(C_c^{-1}-1)}}. \tag{4.11}$$

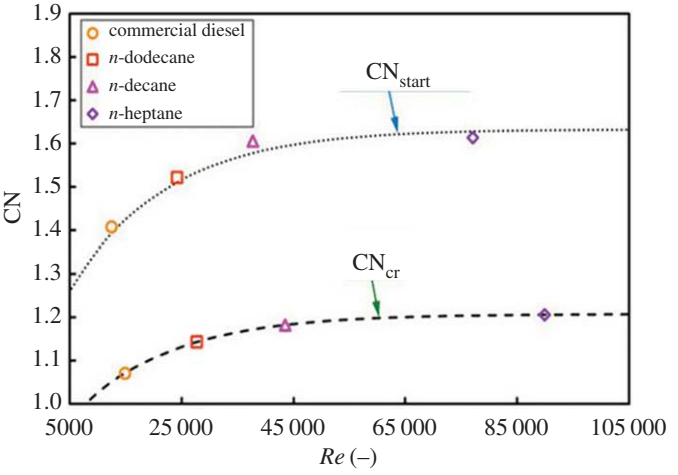

Figure 9. CN_{crit} and CN_{start} versus *Re* [24]. (Online version in colour.)

When A/A_1 cannot be considered null, equation (4.10) should be combined with equation (4.2), in which CN should be substituted by the $(1+\chi)$ quantity for liquid flows. Orifices, which are short nozzles with a length that is shorter than the reattachment distance ($L < L_{sep}$ in figure 1), represent a particular case of straight nozzles. The flow in orifices is detached from the walls, when it leaves section 2. In this case, the evolution from section *C* to section 2 in figure 1 occurs at an almost constant pressure ($p_c \approx p_2$ and $\chi = 0$). As a consequence, $\sqrt{(p_1 - p_c)/p_1 - p_2} \approx 1$ in equation (4.9), which can be simplified as follows:

$$C_d \approx C_c C_v. \tag{4.12}$$

(c) Liquid to cavitating flow transition

If either equation (4.6) or (4.7) is made equal to equation (4.4), it is possible to determine a curve that connects the critical Reynolds number (Re_{cr}) to the critical cavitation number (CN_{cr}), both of which correspond to the choked flow. The pattern of CN_{cr}, with respect to Re_{cr}, is reported in figure 9, on the basis of equations (4.4) and (4.7) for a given nozzle and some fluids: choking obviously occurs when $CN \leq CN_{cr}$. As can be inferred, CN_{start} (experimentally evaluated) is higher than CN_{cr}, this being physically consistent with what can be observed in figure 4*c*.

(d) Velocity coefficient and contraction coefficient

The different formulae that have been reported for both liquid and cavitating flows contain the C_c and C_v coefficients. The velocity coefficient C_v is always close to unity ($C_v \approx 0.97/0.98$) for a developed turbulent flow. The effect of L/d in equation (4.8) is related to C_v, which is also affected by the *Re* number.

Contraction coefficient C_c depends on the shape of the vena contracta section for turbulent flows: the two-dimensional potential flow theory leads to $C_c = \pi/(\pi + 2) \approx 0.611$, an expression that was obtained by Kirchhoff for a free jet (two-dimensional jet) emerging from a rectangular slot orifice. The problem of the calculus of C_c is reduced to a problem of conformal representations between different complex planes, and can be resolved by applying the Schwarz & Christoffel method [73]. As the calculation of C_c is generally difficult, Kirchhoff's determination is often extended approximately to all sharp-edged orifices and also to straight nozzles, regardless of the geometry: the only necessary conditions are that the flow is turbulent and that $A/A_1 \approx 0$.

Many investigations on laminar flows have found that the C_c of either an orifice or a nozzle is proportional to the square root of the Reynolds number, according to

$$C_c \approx \delta\sqrt{Re}, \tag{4.13}$$

where δ is the so-called laminar flow coefficient ($\delta = 0.2$ for circular orifices).

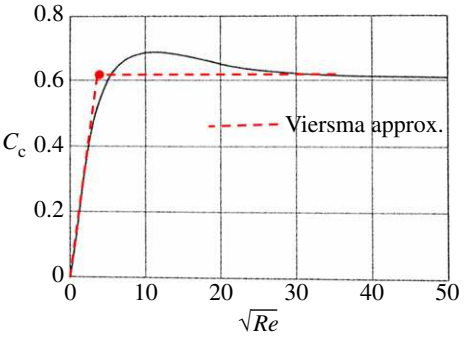

Figure 10. C_c versus Re for an orifice and Viersma asymptotic approximation. (Online version in colour.)

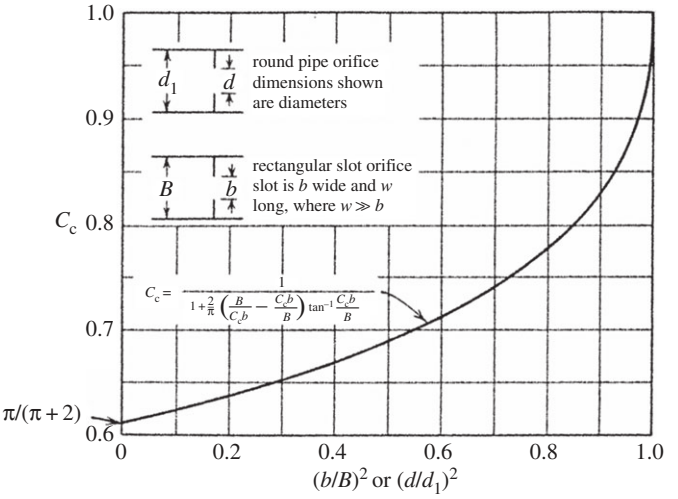

Figure 11. Contraction coefficient as a function of d/d_1.

The laminar-to-turbulent transition Reynolds number (Re_{lt}) can be defined as the value at which equation (4.13) reaches the $\pi / (\pi + 2)$ value (figure 10), that is, when the following relation is in force: $Re_{lt} \approx (0.611/\delta)^2$. For example, it results that $Re_{lt} \approx 9.3$ for $\delta = 0.2$, and the value of Re_{lt} in general increases as δ reduces, but it always remains below 1000. In the Viersma approximated representation [74] (see the dashed line in figure 10), the contraction coefficient is represented by asymptotes that are defined by equation (4.13), and by Kirchhoff's estimation.

Computed expressions of C_c are also available for turbulent flows in those cases in which the A/A_1 ratio cannot be considered null [75]. The following formula is implicit:

$$C_c = \left[1 + \frac{2}{\pi}\left(\frac{d_1}{C_c d} - C_c \frac{d}{d_1}\right) \arctan\left(\frac{C_c d}{d_1}\right)\right]^{-1}, \tag{4.14}$$

where d_1 is the diameter of the upstream duct of the orifice. Figure 11 shows that equation (4.14) also holds for rectangular slot orifices: in this case, b and B replace d and d_1, respectively.

Another possible explicit expression for C_c is the following [43]:

$$C_c = 0.62 + 0.38\left(\frac{A}{A_1}\right)^3. \tag{4.15}$$

Equation (4.15) and figure 11 allow the sensitivity of C_c to A/A_1 to be evaluated: when $(d/d_1)^2 = 0.2$, the difference in the value of C_c, compared with 0.61, which corresponds to

Kirchhoff's determination, is less than 5% in both cases. Therefore, the $\pi/(\pi+2)$ value can be used for C_c when $(d/d_1)^2 \leq 0.2$.

Kirchhoff's determination, as well as equations (4.13)–(4.15), refers to sharp-edged orifices. In the presence of a fillet radius, r_{in}, at the inlet edge of the orifice (see figure 1 at the nozzle inlet), the contraction coefficient can be expressed as follows [43]:

$$\begin{cases} C_{c,radius} = 1 & \dfrac{r_{in}}{d} \geq 0.14, \\ C_{c,radius} = \left[C_c^{-2} - 11.4 \cdot \dfrac{r_{in}}{d} \right]^{-0.5} & \dfrac{r_{in}}{d} < 0.14, \end{cases} \tag{4.16}$$

where C_c can be determined by either equation (4.14) or equation (4.15), or set equal to $\pi/(\pi+2)$. It is worth observing that equation (4.16) predicts the absence of any vena contracta when r_{in} is higher than $0.14d$.

5. Cavitation modelling in engineering systems

Two-phase cavitation models imply that the liquid and vapour phases, which are simultaneously present at the same spatial location in the flow, can be characterized by different velocities, pressures and temperatures, and are therefore not in thermodynamic equilibrium [11]. However, the validation of the additional relationships required for the mathematical closure of these cavitation models, such as the Knudsen–Hertz equation for the vapour flow rate, the velocity slip condition across the bubble interfaces, or the sub-model for the calculus of the gaseous flow rate through the cavity walls, is difficult because of the lack of experimental data that could be used for this purpose.

An alternative modelling approach, which is used extensively in engineering applications for acoustic cavitation, is the single-phase (or homogeneous mixture) concept. Homogeneous-mixture models assume that the vapour and liquid phases are uniformly mixed together, and no clear vapour structures, or inter-phase boundaries, can therefore be simulated in the flow; the dispersed bubbles are rather small, and any significant relative motion is thereby eliminated [76]. The liquid and vapour phases are assumed to be in local thermodynamic equilibrium and, as a consequence, $T_v = T_l := T$. Furthermore, the effects of surface tension, liquid viscosity and velocity slip are neglected at the liquid–vapour boundaries, and the pressure of the mixture is assumed to be equal to the saturation pressure: $p_v = p_l = p(T)$. The physical properties of the mixture are functions both of the properties of the pure phases and of either the void fraction ($\alpha = V_v/V$, where V_v is the volume of the vapour phase and V is the volume of the cavitating mixture) or the mass fraction ($\mu_v = m_v/m$, where m_v is the mass of the vapour phase and m is the mass of the cavitating mixture) of the vapour phase. In the absence of any undissolved gas quantity in the liquid, the density (ρ) and the dynamical viscosity (η) of the cavitating mixture can be expressed as follows [13,77–79]:

$$\begin{cases} \rho = \alpha \rho_v + (1-\alpha)\, \rho_l, \\ \eta = \alpha \eta_v + (1-\alpha)\, \eta_l, \end{cases} \tag{5.1}$$

where ρ_v and η_v are the vapour density and vapour dynamical viscosity (both of which are functions of either temperature or pressure). The vapour can be treated as a perfect gas, i.e. $\rho_v(T) = p(T)/R_v T$, where R_v is the vapour molecular constant, while the liquid phase can be modelled by means of the Tait equation, that is, $\rho_{sat}(T)/\rho_l = 1 - C \ln\{(p_l + B)/[p(T) + B]\}$, where ρ_{sat} is the liquid saturation density at temperature T, and B and C are parameters that depend on the temperature and on the studied liquid fluid, respectively [80]. Another popular expression, which represents a modified version of the original Tait equation, and is referred to as the Tamman equation, is given by $1/E_l = C^*/(p_l + B^*)$, where E_l is the modulus of compressibility of the liquid, and C^* and B^* are quantities that depend on the temperature and on the studied liquid fluid, respectively [81].

A further distinction of homogeneous models can be made between algebraic and differential (or baroclinic) models. Algebraic models are usually applied to acoustic cavitation simulation, whereas hydrodynamic cavitation is often studied by means of baroclinic models.

Algebraic cavitation models assume instantaneous vaporization and condensation processes; a state equation is required to simulate the effect of the pressure on the density of the homogeneous mixture [82]. These models are also known as barotropic equilibrium models, because an *a priori* thermodynamic law of evolution is assumed for the flow. The Wood formula (sometimes also referred to as the Wallis formula), for sound speed, is commonly applied for this kind of model [15,83,84]

$$\frac{1}{\rho a^2} = \frac{\alpha}{\rho_v a_v^2} + \frac{1-\alpha}{\rho_l a_l^2} \quad \text{where} \quad a^2 = \frac{\mathrm{d}p}{\mathrm{d}\rho}, \tag{5.2}$$

where a is the sound speed of the cavitating flow, and a_l and a_v are the sound speeds of the liquid and vapour phases, respectively (both of which are functions of either T or p). However, this expression is related to a pseudo-cavitation evolution (pertaining to gas–liquid mixtures with cavities containing a fixed amount of undissolved gas), and therefore can only be considered as an approximated model when used to simulate liquid–vapour transition phase events [13]. The correct expression, which results from a rigorous calculation of the hyperbolic flow equation eigenvalues of the mass and momentum balance of the mixture, is [85]

$$\frac{1}{\rho a^2} = \frac{\alpha}{\rho_v a_v^2} + \frac{1-\alpha}{\rho_l a_l^2} - \rho\left(\frac{1}{\rho_v} - \frac{1}{\rho_l}\right)\frac{\mathrm{d}\mu_v}{\mathrm{d}p}, \tag{5.3}$$

where $\mu_v = \alpha\rho_v/\rho$. Equation (5.2) or (5.3) should be coupled to the generalized Euler equations in order to guarantee conservation of the mass and momentum of the cavitating mixture. The $\mathrm{d}\mu_v/\mathrm{d}p$ term can be calculated from the energy equation, which is reduced to a state relation, according to the considered thermodynamic evolution [86]. For example, under an isentropic process ($s = \text{const}$), one obtains

$$\left(\frac{\partial \mu_v}{\partial p}\right)_s = \frac{1}{q}\left\{\left[\frac{1}{\rho} - \frac{\mu_l}{\rho_l}(1-\beta_l T)\right] - c_p\frac{\mathrm{d}T}{\mathrm{d}p}\right\}, \tag{5.4}$$

where $c_p = c_{p,v}\mu_v + c_{p,l}\mu_l$ is the specific heat at a constant pressure of the mixture, $c_{p,v}$ and $c_{p,l}$ are the specific heats at a constant pressure of the vapour and liquid phases, $q = q(T)$ is the vaporization heat of the liquid, and ρ_l, $\beta_l = -1/\rho_l\,(\partial\rho_l/\partial T)_p$ and $\mu_l = 1-\mu_v$ are the density, thermal expansivity and mass fraction of the liquid phase, respectively.

The assumption of isothermal evolution in the cavitation region leads to drastic simplifications. In fact, an isothermal phase change is also an isobaric process in equilibrium thermodynamics, and the $(\partial\mu_v/\partial p)_T$ derivative in equation (5.3) tends to be infinite, because a finite change in μ_v can take place with a null pressure variation: as a consequence, a tends to zero. Although the mixture sound speed is not equal to zero for an isentropic process, it takes on very low values [10], and remains around $1\,\mathrm{m\,s^{-1}}$ for $\alpha > 0$ [87]. This is why the thermodynamic evolution does not affect acoustic cavitation dynamics to any great extent.

The advantage of adopting equations (5.2) and (5.3) is that they can easily be integrated in an algebraic relation, i.e. $p = p(\rho)$, once they have been coupled to the expression of ρ given by equation (5.1), and to the right formula of $\partial\mu_v/\partial p$ [10,13]. On the other hand, algebraic models are unable to describe the baroclinic nature of cavitating flows, because the void fraction variation, at a given instant and point of the cavitation region, cannot depend on the time history of the whole flow [51].

Homogeneous-mixture differential cavitation models are able to include the baroclinic nature of cavitating flows. The void fraction is usually evaluated by means of a standard convective transport equation, which is added to the mass conservation and momentum balance equations of the cavitating mixture. Moreover, it can be proposed in the following conservative form for a

one-dimensional flow:

$$\frac{\partial(\rho_v\alpha)}{\partial t}+\frac{\partial(\rho_v\alpha\, u)}{\partial x}=\Gamma \quad \Leftrightarrow \quad \frac{\partial\alpha}{\partial t}+\frac{\partial(\alpha\, u)}{\partial x}=\frac{\Gamma}{\rho_v}, \tag{5.5}$$

where Γ is the vapour source term, which should be modelled *a priori*.

Variable α appears in state relations, such as equations (5.1)–(5.3), in equilibrium barotropic models, whereas it is the unknown variable of a partial differential equation in baroclinic models: in the latter models, at a certain point and time instant, the value of α depends on the time evolution of the field of this variable, and on both the boundary and initial conditions.

The baroclinic models are usually based on the assumption of isothermal flow and incompressibility of the vapour and liquid phases [88]. The compressibility of the cavitating fluid, that is, the variation in its density ρ, is in fact due to the changes in the vapour fraction (α), while the changes in ρ_v and ρ_l, which are caused by pressure variations, only play a marginal role.

So far, most efforts have been focused on correctly evaluating Γ [89–92], the formulation of which represents the main difficulty in this procedure (this term is absent in barotropic models). Various heuristic expressions can be found for term Γ in the literature: the formulae are usually distinct for evaporation and condensation processes. A popular and simple model of Γ [88] is given by [93]

$$\begin{cases}\Gamma=\dfrac{1}{\tau_{ev}}\dfrac{U_\infty}{L_\infty}\rho_l(1-\alpha)\dfrac{(p_v-p)}{1/2\,2\rho_\infty U_\infty^2} & \text{for } p<p_v,\\[2ex] \Gamma=\dfrac{1}{\tau_{cond}}\dfrac{U_\infty}{L_\infty}\alpha\rho_v\dfrac{(p_v-p)}{1/2\rho_\infty U_\infty^2} & \text{for } p>p_v,\end{cases} \tag{5.6}$$

where L_∞ and U_∞ are the characteristic length and velocity, respectively, of the flow, ρ_∞ is a characteristic density of the flow (for instance the asymptotic value), and τ_{ev} and τ_{cond} are time constants for vapour formation and liquid reconversion, respectively.

Other models similar to this one are reported in [90,92,94]. The expression of the Wood sound speed formula, which was derived in the context of barotropic models, can also be used to model the source term Γ [76].

Another class of Γ models includes laws for the evolution of the vapour bubble radius [95]. The following cavitation model is reported as it has frequently been used in the literature [7,78]:

$$\begin{cases}\Gamma=\dfrac{(1-\alpha)\rho_l\rho_v}{\rho}\dfrac{n_0}{1+n_0V_B}\dfrac{dV_B}{dt}\text{sign}(p_v-p),\\[2ex] V_B=\dfrac{4}{3}\pi R^3 \quad \alpha=\dfrac{n_0V_B}{1+n_0V_B} \quad \dfrac{dR}{dt}=\pm\sqrt{\dfrac{2}{3}\dfrac{|p_v(T)-p|}{\rho_l}}.\end{cases} \tag{5.7}$$

Parameter n_0 is the number of cavitation bubbles per unit volume of the liquid phase (n_0 coincides with the number of initial nuclei) and $R(t)$ is the instantaneous bubble radius (all the vapour bubbles should have the same diameter at a certain instant). The initial size of the cavitation nuclei (R_0) and n_0 are constant parameters in this model, and they allow a rough estimation of the effect of the liquid quality on cavitation to be made. These parameters are tunable and should be fitted to the experimental data. For example, it has been shown that when n_0 varies from 10^{12} to 10^{14} nuclei m^{-3} [96], and R_0 varies from 1 to 100 μm, accurate results can be obtained for the simulation of water in small-size nozzles.

The dR/dt law in equation (5.7) is founded on the inertially controlled simplified solution of the Rayleigh–Plesset equation for bubble dynamics [97] (see §5a). The bubble grows if the pressure is less than the vaporization pressure, that is, $p<p_v$, and collapses when $p>p_v$. Bubble collapse, as modelled by the complete Rayleigh differential equation, should be much more rapid than bubble growth, but equation (5.7) does not differentiate between the expressions of dR/dt for bubble growth and collapse [98].

It is also possible to take into account the effect of bubble coalescence at large α values by applying the following formula to evaluate n, which, in this alternative formulation, replaces n_0

in equation (5.7) [97,99]:

$$n = \begin{cases} n_0 & \alpha \leq 0.5, \\ 1 + 2(n_0 - 1)(1 - \alpha) & \alpha > 0.5. \end{cases} \tag{5.8}$$

In the reported Γ models, the difference between liquid and saturation pressure, that is, the term $(p_v - p)$, is generally considered to be the driving force behind the formation and destruction of the vapour phase. In general, simplified baroclinic models assume the same average concentration of bubbles (n) throughout the flow field, and do not consider any distribution of the bubble population with respect to the radius.

The main advantage of baroclinic models, based on simplistic expressions that can be obtained from the bubble dynamics theory, such as equation (5.7), is that they offer the possibility of taking into account liquid quality scales, whereas this is not possible in equation (5.6), or in homogeneous-mixture algebraic models. This typology of baroclinic models has been found to be robust and efficient for the prediction of cavitation flows, and is not as computationally expensive as more sophisticated baroclinic models, such as those that solve the Rayleigh–Plesset equation for bubble dynamics.

(a) The Rayleigh–Plesset equation for single-bubble dynamics

The Rayleigh–Plesset equation is obtained by applying the correct boundary conditions, which are derived due to the presence of a bubble, to the Navier–Stokes equations written for the incompressible, radially symmetric, liquid flow that surrounds the bubble [100]. The Rayleigh–Plesset equation can be presented in the following form [9]:

$$\left(R \cdot \ddot{R} + \frac{3}{2}\dot{R}^2\right) + 4\nu_l \frac{\dot{R}}{R} + \frac{2}{\rho_l}\frac{s}{R} = \frac{p_B - p_l}{\rho_l}, \tag{5.9}$$

where $\nu_l = \eta_l / \rho_l$ is the kinematic viscosity of the liquid, p_B is the pressure inside the bubble, p_l is the liquid pressure at the bubble surface and s is the surface tension.

The Rayleigh–Plesset equation accounts for the effects of inertia, viscosity and the surface tension of the bubbles, and it can be incorporated in one-, two- and three-dimensional partial differential equation models to simulate cavitating flows [53,101,102]. As the Rayleigh–Plesset equation causes the bubble growth and collapse rates to be time dependent, it is suitable for the simulation of transient structures in cavitation flows.

Different and more sophisticated variants of equation (5.9) are available in the literature to take into account other effects, such as: the evaporation and diffusion flow rates of vapour and gas through the bubble walls [79,103,104], temperature discontinuity at the bubble surface between the aeriform constituents and the liquid phase [105], the kinematic slip condition between the liquid and vapour phases [105,106] as well as liquid compressibility [107,108]. The temperature, pressure and velocity differences between the different phases can be simulated in two-phase models, in which a Rayleigh–Plesset-type equation is coupled to the mass and momentum conservation and partial differential equations for each distinct phase [11]. However, the form of the Rayleigh–Plesset equation given by equation (5.9) can also be adopted in sophisticated baroclinic differential models.

The concept of Blake's radius is reviewed hereafter, as it is important to understand the sensitivity of cavitation inception to the bubble dimensions, when a Rayleigh–Plesset equation is used. The pressure, p_B, inside a spherical bubble of small radius R is related to the pressure, p_l, of the outside liquid, through a normal stress balance across the bubble surface. If the no-slip condition is applied, that is, $u_B \approx u_l$, where u_l is the liquid velocity at the bubble surface and u_B is the fluid velocity inside the bubble, and the liquid viscosity is neglected ($\eta_l \approx 0$), the following relation is obtained for quasi-static equilibrium conditions:

$$p_B - p_l = \frac{2s}{R}, \tag{5.10}$$

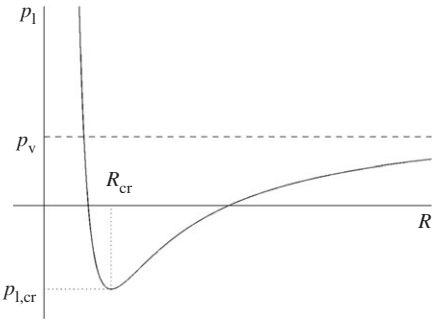

Figure 12. Blake's radius and critical liquid pressure.

where $p_B = p_g + p_v(T)$, and p_g is the Dalton pressure of the undissolved gas within the bubble. If an isothermal flow is assumed, p_v is a constant, and p_g can be expressed using Boyle's law,

$$p_g = p_{g,0}\frac{R_0^3}{R^3}, \tag{5.11}$$

where R_0 is the value of the bubble radius at its initial conditions, that is, when $p_l = p_\infty$ and $p_{g,0} = p_\infty + 2s/R_0 - p_v$. Finally, bearing in mind this relation for $p_{g,0}$, the following expression can be obtained by combining equations (5.10) and (5.11):

$$p_l = p_v + \frac{\tilde{G}}{R^3} - \frac{2s}{R}, \tag{5.12}$$

where $\tilde{G} = R_0^3(p_\infty - p_v + 2s/R_0)$ is a constant term. The r.h.s. of equation (5.12) has been plotted in figure 12 as a function of R, and the resulting curve shows a minimum point ($p_{l,cr}$) in correspondence to a critical radius, which has been labelled R_{cr}, and is referred to as the Blake radius:

$$R_{cr} = \left(\frac{3\tilde{G}}{2s}\right)^{1/2} \qquad p_{l,cr} = p_l(R_{cr}) = p_v - \left(\frac{32s^3}{27\tilde{G}}\right)^{1/2}. \tag{5.13}$$

By combining these two expressions, it is possible to express the Blake radius through the following final formula, which is usually reported in the literature [9,109]:

$$R_{cr} = \frac{4s}{3(p_v - p_{l,cr})}. \tag{5.14}$$

Equation (5.12) yields two possible solutions for radius R: nuclei with a lower radius than the Blake radius are stable to small disturbances for p_l values below vapour pressure p_v, but above the critical value ($p_{l,cr}$), whereas nuclei with $R > R_{cr}$ are unstable to small disturbances and grow explosively, thus giving rise to cavitation. If liquid pressure (p_l) is lowered to a value below the corresponding critical pressure $p_{l,cr}$, no equilibrium radius exists, and the nucleus grows explosively. In other words, $p_{l,cr}$ is the value below which cavitation surely occurs, regardless of the original value of the nucleus radius.

In the presence of a real liquid, where gaseous nuclei of different sizes exist simultaneously, it is important to consider the fluctuations in the pressure and the number of nuclei with a larger radius than the Blake radius. As far as the definition of cavitation inception in the fluid is concerned, it is relatively difficult to consider the explosive bubble growth that is accidentally caused by large freestream nuclei and/or large pressure fluctuations as the cavitation inception point [110]. Cavitation inception is verified when repeatable vapour bubble occurrences take place, that is, when the number of vapour bubble occurrences per unit time exceeds a certain threshold value.

When the pressure changes undergone by the bubble are no longer quasi-static, a more detailed model than that based on equation (5.10), which can also take the damping term into consideration, should be introduced to determine cavitation inception [111].

Finally, it should be pointed out that the phenomena related to the Blake radius cannot be studied when the surface tension effect is not included in the simplified Rayleigh–Plesset equation. This is, for example, the case of the baroclinic model given by equation (5.7). In this case, cavitation inception takes place as soon as $p < p_v$, regardless of the R_0 value. As a consequence, the model in equation (5.7) cannot correctly simulate the effect of the liquid quality, related to the initial dimension of the nuclei on cavitation inception [62].

(b) Homogeneous and heterogeneous nucleation in two-phase models

The Rayleigh–Plesset equation has been applied extensively to describe the growth and collapse dynamics of single, spherical, vapour–gas bubbles immersed in unlimited liquid fields [9,112], when the liquid pressure reduces to the vapour tension level. Some basic assumptions of the single-bubble model become critical in many real situations. As hydraulic engineering systems are confined, the assumption of spherical symmetry in the liquid field is critical for cavities located near the container walls. Furthermore, when strong pressure wave dynamics is present, as is the case in acoustic cavitation, or high-pressure gradients are present in steady flows, as occurs in nozzles, the liquid field cannot be considered at rest before vaporous bubbles begin to form. Above all, the application of the Rayleigh–Plesset approach to real liquids requires accurate expressions of the $N(R)$ nucleus-size spectral distribution function ($N\mathrm{d}R$ gives the number of gaseous nuclei with a radius from R to $R + \mathrm{d}R$ per unit of liquid volume). In fact, the nuclei in liquid flows have a vast range of diameters, and, as shown in the previous subsection, the size of the nucleus can be a decisive parameter in the determination of the fate of a bubble.

The following general lognormal distribution can be applied to approximately describe the nucleus-size spectral distribution [113]:

$$N(R_0) = \frac{\mathrm{d}n_0}{\mathrm{d}R} = \frac{\psi}{\sqrt{2\pi}\,\Sigma} \exp\left[-\frac{1}{2}\left(\frac{\log(R_0/\xi)}{\Sigma}\right)^2\right], \tag{5.15}$$

where Σ, ψ and ξ are fitting parameters, which depend on the considered fluid (ξ and Σ represent the average radius and the standard deviation of the distribution, respectively). Each nucleus evolves according to the Rayleigh–Plesset equation, that is, the radius (R_0) of the considered nucleus is used as the initial condition to solve equation (5.9). The N distribution can be related to the initial void fraction of the undissolved gas ($\alpha_g = V_g/V$) through the following equation:

$$\alpha_{g,0} = \frac{\int_{R_{min}}^{R_{max}} V_B(R) N(R)\,\mathrm{d}R}{1 + \int_{R_{min}}^{R_{max}} V_B(R) N(R)\,\mathrm{d}R}, \tag{5.16}$$

where $V_B = 4/3\pi R^3$ and R_{min} and R_{max} are the minimum and maximum radii of the nuclei population.

Simplistic power-law approximations of the nucleus-size distribution function, such as the following one, are often applied for engineering and practical calculations [100,114]:

$$N(R_0) = \frac{b}{R_0^m}, \tag{5.17}$$

where b and m are fixed parameters. The subsequent values have been selected to describe measurements in water over the $R_{min} = 10\,\mu m$ to $R_{max} = 200\,\mu m$ range:

$$m = 4 \quad b = \frac{3\alpha_0}{4\pi\,(1-\alpha_0)\ln(R_{max}/R_{min})}. \tag{5.18}$$

Although equations (5.17) and (5.18) allow experimental results to be predicted, reliable expressions, regarding the spectral distribution of nucleus sizes, can only be derived on the basis of experimental data concerning the specific application. The lack of generality represents a serious drawback for cavitation models based on theoretical expressions of $N(R)$.

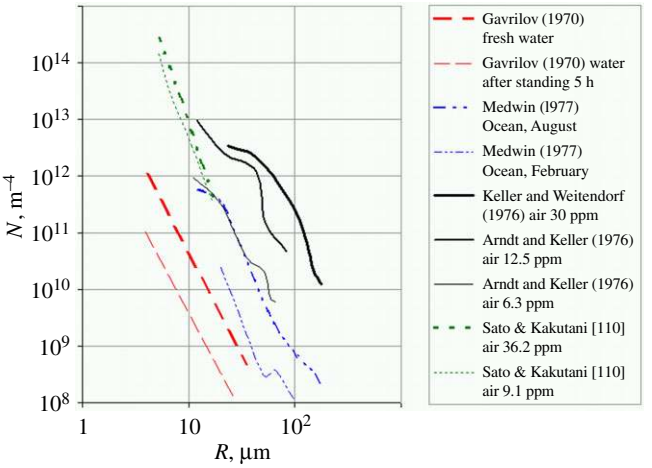

Figure 13. Measurement of $N(R)$ in water with different purities ($T = 293$ K) [110]. (Online version in colour.)

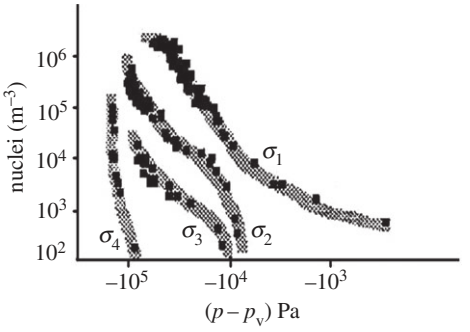

Figure 14. Activated nuclei as a function of water tensile strength for a ship propeller [21]; curve σ_1 refers to a high content of large nuclei, curve σ_2 refers to a high content of medium-sized nuclei; curve σ_3 refers to a low content of medium-sized nuclei and curve σ_4 refers to heavily degassed water.

Experimental methods have been developed to evaluate the density distribution function of the nuclei [115]; these methods are based on acoustic and light scattering techniques, on holograms of small volumes in the flow (the most reliable method), on phase Doppler anemometers, on cavitation susceptibility meters (the most popular method) and on centrebody Venturi tube methods [116]. Nucleus-size spectral distribution functions obtained by means of experimental techniques are reported in figure 13. In general, the trend of N with respect to R can vary from liquid to liquid, and can depend on the concentration of small contaminant particles, on the quantity of dissolved gas in the liquid, and on the pressure and temperature conditions.

Figure 14 shows the tensile strength of water, i.e. $(p - p_v) < 0$ (tension is here considered negative), as a function of the number of activated nuclei for different average radii of the initial freestream nuclei and for different nucleus-size spectral distribution functions [21].

The role of freestream cavitation nuclei has emerged to be of primary importance for cavitation inception from an analysis of the influence of the quality of water [21,117]. Four different curves have been generated with the data obtained from the Venturi tube measuring technique [118]. These curves refer to strongly degassed water (curve σ_4), to a low injection of medium-sized nuclei (σ_3), to a large injection of medium-sized nuclei (σ_2) and to a large injection of large nuclei (σ_1). By injecting medium-sized nuclei, and considering both a low content and a high content, it is possible to examine the influence of the number of nuclei of a given size on the cavitation inception characteristics.

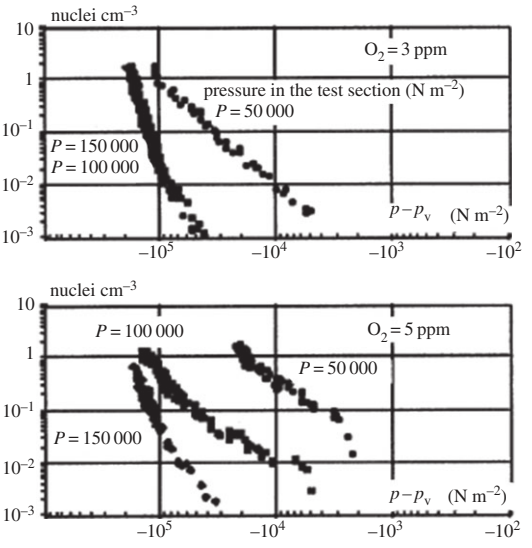

Figure 15. Effect of water tensile strength on the number of activated nuclei for different dissolved gas fractions and different pressure conditions [21].

As can be inferred, the higher either n_0 or the average radius of the nuclei, the lower the modulus of the tensile strength of the liquid, that is, the higher the value of p at which liquid rupture occurs and cavitation develops. Hence, the values of CN_{start} and CN_{cr} increase as either the number of gaseous nuclei per unit volume of liquid increases or larger average radii of the nucleus-size spectral distribution function are considered. In particular, when a sufficient number of large nucleation sites is present, liquid rupture and explosive vaporization tend to occur as soon as the liquid pressure reaches the vapour tension level [119], and the isobaric–isothermal Clausius–Clapeyron equilibrium transition therefore results to be an accurate approximation of cavitation evolution (the liquid tensile strength can be considered negligible in these cases).

It is worth observing that the specific pattern of the curves plotted in figure 14, and therefore the influence of the fluid quality on cavitation, also depends on the analysed typology of cavitation: the effect of the number and size of the nuclei can be different for blade surface cavitation, tip vortex cavitation and acoustic cavitation events [21].

The dissolved air content was kept constant during all the tests in figure 14. Figure 15 shows that the concentration of activated nuclei reduces for a fixed tensile strength as the mass fraction of dissolved gas (oxygen) in the liquid decreases. Furthermore, figure 15 points out how the initial quantity of gas dissolved in the liquid can affect the $N(R)$ curve [111]; in fact, the size and number of freestream nuclei dispersed within the flow can also be related to the initial concentration of dissolved gas.

6. Physics of cavitation and comparison with supersonic flows

Figures 16 and 17 report the numerical distributions of pressure p (with a thick solid line), void fraction α (with a dashed line) and volumetric flow rate Q (with a thin solid line) along a pipe of length L that connects one pumping unit of an in line-pump (located at $x/L = 0$) to an automatic injector (located at $x/L = 1$) for a certain time instant (θ is the pumpshaft rotational angle and θ_0 is a reference value). A barotropic cavitating flow has been considered to model the pump-to-injector pipe, and equation (5.3) has been used to calculate the sound speed.

Figure 16 refers to an acoustic cavitation event that has arisen at the pipe inlet ($x/L \approx 0$), whose effect has extended along the pipe. A spill port, which connects the high-pressure fuel to the tank, opens in the pumping chamber at the end of the pump delivery phase, and the thus induced

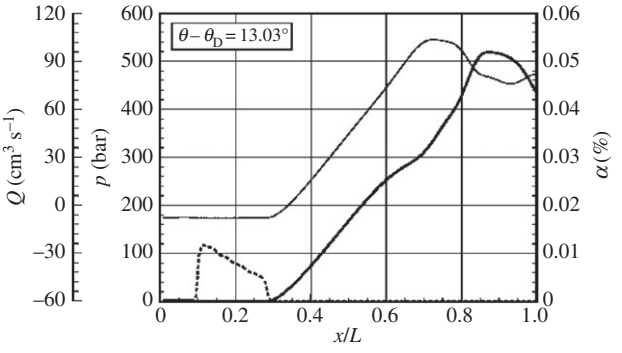

Figure 16. Cavitation inception and development.

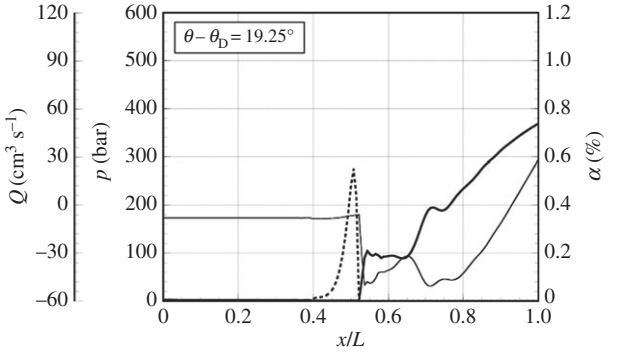

Figure 17. Cavitation desinence.

depression drains fuel from the beginning of the pipe, so that Q is negative for $0 < x/L < 0.3$. This rarefaction gives rise to a cavitation zone in which $\alpha > 0$ [10], and it occurs at the tail of a compression wave, which was previously generated by the pump-delivered fuel, and which has just reached the injector in figure 16.

Figure 17 refers to an acoustic cavitation desinence phenomenon that occurs after the end of the injection phase. The nozzle closure determines a water hammer event within the injector, and a compression wave that travels from the injector toward the pump is generated. The cavitation region that had previously formed (figure 16) is progressively swept away by this compression wave.

The transition from liquid to vapour that can be observed in figure 16 occurs at the border on the right of the cavitation zone ($x/L \approx 0.3$), with an almost continuous and gradual change in the flow properties, whereas the passage from vapour to liquid shown in figure 17 takes place at the boundary on the right of the cavitation zone, with a shock-like transition in the flow properties [85].

The scheme in figure 18*a* expands the pressure (solid line) and void fraction (dashed line) spatial distributions close to the boundary between the cavitating and liquid regions, at a certain time instant, for a case like the one shown in figure 16 (cavitation inception). The abscissas x_i and x_{i+1} indicate grid nodes of the computational mesh, while p_i and p_{i+1}, and α_i and α_{i+1} are the pressure and void fraction values at these nodes, respectively.

The characteristic lines of the generalized Euler equations that govern the flow have been schematically plotted outside the (x_i, x_{i+1}) interval in figure 18*b*. For the sake of simplicity, an isothermal evolution of the liquid–vapour mixture has been considered in figure 18*b*, even though the main conclusions remain in force, regardless of which evolution law is selected. Because the sound speed value falls from a_l to 0 in the passage from liquid to cavitating flow, the characteristics belonging to the region subjected to cavitation and to the zone of the pure liquid

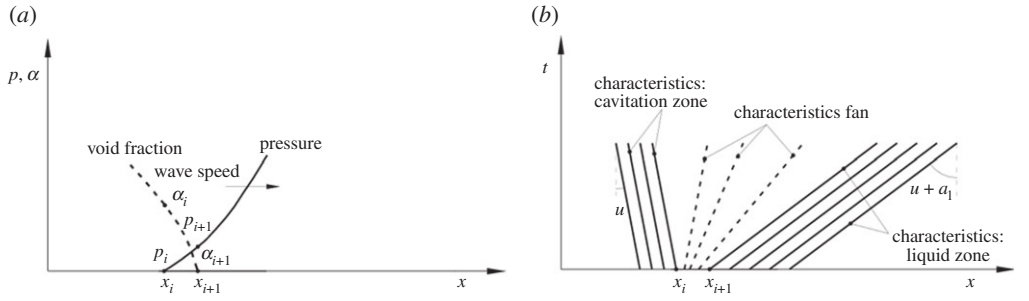

Figure 18. Analysis of cavitation inception. (*a*) Pressure and void fraction distribution. (*b*) Characteristic lines related to the $(u + a)$ eigenvalue.

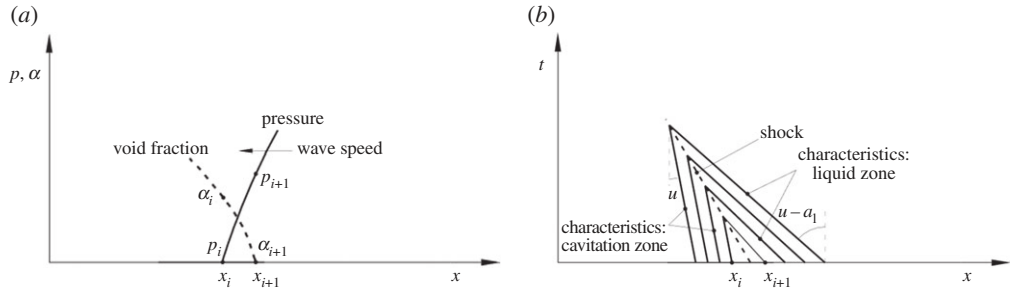

Figure 19. Analysis of cavitation desinence. (*a*) Pressure and void fraction distribution. (*b*) Characteristic lines related to the $(u - a)$ eigenvalue.

diverge and give rise to a fan [10,85]. Therefore, no shock occurs in the flow during cavitation inception, and a continuous transition from a subsonic to a hypersonic flow takes place in the (x_i, x_{i+1}) interval: the sound speed reduces from a_1, which is typical of a liquid flow where $Ma_1 \ll 1$, to very low values in the cavitation zone where $Ma > 1$.

Figure 19*a* schematically reports the numerical distributions of the pressure and void fraction, at a certain time instant, for a cavitation desinence event; it qualitatively reproduces what occurs on the right of the cavitation region boundary in figure 17. Furthermore, figure 19*b* plots the characteristics that correspond to the $u - a_1$ and u eigenvalues, pertaining to the liquid and cavitation zones, respectively, outside the (x_i, x_{i+1}) interval. These characteristics converge and intersect, and thus give rise to a shock wave, as can also be verified by observing the pressure wavefront in figure 17. Cavitation desinence in fact occurs as a result of a hypersonic–subsonic shock: the supersonic flow at a pipe location within the vaporization region becomes subsonic, as soon as the liquid compression wave proceeds across this location. The Mach number, in the vapour-to-liquid transition phase, primarily varies as a consequence of reversible changes in the sound speed, rather than as a result of dramatic variations in the fluid velocity. This Mach variation is rather different from that of aerodynamic shocks, where the irreversible step variations in the velocity are the most relevant aspect in determining the changes in the Mach number. Hence, an isentropic law of evolution can also be used to describe cavitation collapse [10].

The general analogy between supersonic flows and cavitation is enforced by considering the occurrence of the choked flow in nozzles that are subjected to hydrodynamic cavitation. As already mentioned, a choked flow rate can be observed in figure 5, when $\Delta p^{1/2} = (p_1 - p_2)^{1/2}$ increases beyond a certain threshold. Although the order of magnitude of this threshold can vary to a great extent for different cases [24,62], the quantity value $(\mathrm{CN_{cr}})^{1/2}$ is usually in the 1.1–1.7 range for different fluids and nozzle geometries [71,120].

Figure 20 refers to STAR-CCM+ simulation results obtained with a three-dimensional cavitation baroclinic model, like the one shown in equations (5.5) and (5.6), for a straight nozzle

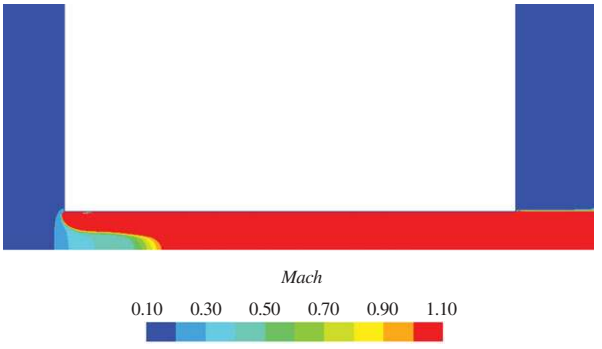

Figure 20. Choking-flow conditions (Mach number field, CN ≈ 1.29).

that connects two water reservoirs: $CN_{cr} = 1.30$ and the plotted data correspond to a flow choking condition (CN ≈ 1.29).

The choked flow, due to cavitation, starts to occur as soon as at least a critical section (A_{cr}) exists, over which $Ma \geq 1$ for all the points [62]; this definition is in line with that of a choked flow in aerodynamics. The occurrence of $\alpha > 0$ at all the points of A_{cr} is a necessary condition to make a diminish in equation (5.2) or (5.3), and thus to obtain a sonic flow at all the points of section A_{cr}.

As the steady-state fluid velocity is directed towards the nozzle exit, the effects of any change in the downstream reservoir pressure (p_2) cannot influence the fluid properties in the field located upstream of A_{cr} when the flow is supersonic throughout an entire section or in a portion of the nozzle (as in figure 20). The mass flow rate under choking conditions is controlled by the pressure drop between the upstream reservoir (p_1) and the section in which cavitation appears (p_v), while it is not correlated well with the pressure drop ($p_1 - p_2$) over the nozzle [39].

The characterization provided for the choked flow, due to cavitation, theoretically makes this kind of regime clearly distinct from cavitation inception and supercavitation, even though the hydraulic criteria used to detect cavitation inception are often based on the detection of mass flow choking [39], or are empirically expressed in terms of a certain percentage reduction in the flow rate compared with the choking conditions [121,122]. On the other hand, the instability that occurs in transitional cavitation, within the $L_{cav}/L \approx 0.25$–0.35 range (see §3), makes it practically difficult to distinguish between the condition at which cavitation spreads over a critical section (choking) and the condition at which cavitation reaches the nozzle exit (supercavitation).

7. Conclusion

The fluid dynamical effects and the modelling aspects of vaporous cavitation in engineering systems have been reviewed. The performance of hydraulic power systems can be affected by both acoustic and hydrodynamic cavitation. Acoustic cavitation is induced by rarefaction waves propagating throughout the liquid region in hydraulic power systems, whereas hydrodynamic cavitation occurs when a pressure reduction to the vapour tension level is caused by the geometrical layout of the flow passages.

Acoustic cavitation affects the wave propagation speed in the pipes of the engineering systems in which it takes place. The sound speed of cavitating flows is close to zero, regardless of the selected thermodynamic evolution. The Wood formula is commonly applied to model the sound speed in vaporous cavitation sections, because it is easy to implement, and it gives satisfactory results, but this formula is not physically consistent with the simulation of phase transition processes. More accurate expressions of the sound speed, which include a vapour source term, have been developed on the basis of the energy equation, which is reduced to a state relation according to the selected thermodynamic evolution law.

Hydrodynamic cavitation can significantly affect the permeability of nozzles and orifices, which are typical components of hydraulic power systems. When secondary-scale effects can be

neglected, it is possible to consider hydrodynamic similarity in order to experimentally study miniaturized layouts through the realization of large-scale cylindrical nozzles that facilitate the visualization of the phenomena. The currently adopted two- and three-dimensional computation approaches to hydrodynamic cavitation are still not at a fully mature stage, as is the case for one-phase acoustic cavitation calculations, and they still need improvements, even though some two-dimensional and three-dimensional analyses have started to appear over the last few years. The discharge coefficient of straight nozzles can generally be expressed as a function of Re and of L/d in the turbulent liquid field, whereas it mainly depends on CN when cavitation develops. The inception of hydrodynamic cavitation leads to an increase in the nozzle discharge coefficient, compared with the liquid flow, because the very small number of bubbles located at the inlet corner of the nozzle is able to smooth the internal flow, and thus improve the discharge coefficient. This local maximum point in the C_d versus CN curve is a useful criterion to detect cavitation inception.

As soon as flow choking occurs, the mass flow rate begins to be affected only by the pressure in the upstream reservoir. Choking due to cavitation begins as soon as at least a critical section of the nozzle exists, over which $Ma \geq 1$ for all the points. The occurrence of $\alpha > 0$ at all the points of a critical section is a necessary condition to make the sound speed diminish, and thus to obtain a sonic flow at all the points in that section. This definition of choking due to cavitation is in line with that of a choked flow in aerodynamics. Furthermore, this definition makes choking clearly distinct from supercavitation, which occurs when the vapour region reaches the nozzle exit, and there is a clear vapour–liquid separation layer. However, the abrupt change, due to instability, that suddenly leads from $L_{cav}/L \approx 0.25-0.35$ to $L_{cav}/L \approx 1$ often makes it difficult to distinguish between choked flow and supercavitation.

Barotropic homogeneous mixture models are usually applied for the modelling of acoustic cavitation, while baroclinic homogeneous mixture models are the most frequently used for hydrodynamic cavitation. It could be of interest to incorporate accurate nucleus-size spectral distributions and the complete Rayleigh–Plesset equation into two-phase cavitation models, in order to improve the simulation of bubble dynamics (for example the instability related to the Blake radius), and the simulation of the effect of liquid quality on hydrodynamic cavitation. However, there is still much work to be done to derive reliable nucleus-size spectral distribution functions for engineering fluids.

Competing interests. No competing interests are declared.
Funding. No funding has been provided for this study.

References

1. Fortes-Patella R, Choffat T, Reboud JL, Archer A. 2013 Mass loss simulation in cavitation erosion: fatigue criterion approach. *Wear* **300**, 205–215. (doi:10.1016/j.wear.2013.01.118)
2. Petkovsek M, Dular M. 2013 Simultaneous observation of cavitation structures and cavitation erosion. *Wear* **300**, 55–64. (doi:10.1016/j.wear.2013.01.106)
3. Tsujimoto Y. 2006 Flow instabilities in cavitating and non-cavitating pumps. In *Design and analysis of high speed pumps*, pp. 7-1–7-24. Educational Notes RTO-EN-AVT-143, Paper 7. Neuilly-sur-Seine, France: RTO. See http://www.rto.nato.int/abstracts.asp.
4. Tsujimoto Y, Kamijo K, Brennen CE. 2001 Unified treatment of flow instabilities of turbomachines. *J. Propul. Power* **17**, 636–643. (doi:10.2514/2.5790)
5. Pouffary B, Fortes-Patella R, Reboud JL, Lambert PA. 2008 Numerical simulation of 3D cavitating flows: analysis of cavitation head drop in turbomachinery. *ASME Trans. J. Fluids Eng.* **130**, 061301. (doi:10.1115/1.2917420)
6. Wosnik M, Arndt REA. 2013 Measurements in high void fraction bubbly wakes created by ventilated supercavitation. *ASME Trans. J. Fluids Eng.* **135**, 011304. (doi:10.1115/1.4023193)
7. Roohi E, Zahiri AP, Passandideh-Fard M. 2013 Numerical simulation of cavitation around a two-dimensional hydrofoil using VOF method and LES turbulence model. *Appl. Math. Modell.* **37**, 6469–6488. (doi:10.1016/j.apm.2012.09.002)
8. Tomov P, Khelladi S, Ravelet F, Sarraf C, Bakir F, Vertenoeuil P. 2016 Experimental study of aerated cavitation in a horizontal Venturi nozzle. *Exp. Therm. Fluid Sci.* **70**, 75–85. (doi:10.1016/j.expthermflusci.2015.08.018)

9. Brennen CE. 1995 *Cavitation and bubble dynamics*. Oxford, UK: Oxford University Press.
10. Catania AE, Ferrari A, Spessa E. 2008 Temperature variations in the simulation of high-pressure injection system transient flows under cavitation. *Int. J. Heat Mass Transfer* **51**, 2090–2107. (doi:10.1016/j.ijheatmasstransfer.2007.11.032)
11. Ferrari A. 2010 Modelling approaches to acoustic cavitation in transmission pipelines. *Int. J. Heat Mass Transfer* **53**, 4193–4203. (doi:10.1016/j.ijheatmasstransfer.2010.05.042)
12. Vanhille C, Campos-Pozuelo C. 2012 Acoustic cavitation mechanism: a nonlinear model. *Ultrason. Sonochem.* **19**, 217–220. (doi:10.1016/j.ultsonch.2011.06.019)
13. Catania AE, Ferrari A, Manno M, Spessa E. 2006 A comprehensive thermodynamic approach to acoustic cavitation simulation in high-pressure injection systems by a conservative homogeneous barotropic-flow model. *ASME Trans. J. Eng. Gas Turbines Power* **128**, 434–445. (doi:10.1115/1.2056007)
14. Catania AE, Ferrari A, Spessa E. 2009 Numerical-experimental study and solutions to reduce the dwell time threshold for fusion-free consecutive injections in a multijet solenoid-type CR system. *ASME Trans. J. Eng. Gas Turbines Power* **131**, 022804.
15. Chaudhry MH, Bhallamudi SM, Martin CS, Naghash M. 1990 Analysis of transient pressures in bubbly, homogeneous, gas-liquid mixtures. *ASME J. Fluids Eng.* **112**, 225–231. (doi:10.1115/1.2909392)
16. Shu J-J, Edge KA, Burrows CR, Xiao S. 1993 Transmission line modelling with vaporous cavitation. In *Proc. 1993 ASME Winter Annu. Meeting, New Orleans, LA, 28 November–3 December 1993*, paper 93-WA/FPST-2. New York, NY: American Society of Mechanical Engineers.
17. Schmidt DP, Rutland CJ, Corradini ML, Roosen P, Genge O. 2000 Cavitation in two-dimensional asymmetric nozzles. *SAE Trans. J. Engines* **108**, 613–629.
18. He Z, Guo G, Tao X, Zhong W, Leng X, Wang Q. 2016 Study of the effect of nozzle hole shape on internal flow and spray characteristics. *Int. Commun. Heat Mass Transfer* **71**, 1–8. (doi:10.1016/j.icheatmasstransfer.2015.12.002)
19. Catania AE, Dongiovanni C, Mittica A. 1992 Implicit numerical model of a high-pressure injection system. *J. Eng. Gas Turbines Power* **114**, 534–543. (doi:10.1115/1.2906622)
20. Arcoumanis C, Gavaises M, Abdul-Wahab E, Moser V. 1999 Modeling of advanced high-pressure fuel injection systems for passenger car diesel engines. *SAE Trans. J. Engines* **108**, 1347–1362.
21. Gindroz B. 1998 Cavitation nuclei and cavitation inception of marine propellers: state of the art at the dawn of 21st century. *JSME Int. J. Ser. B* **41**, 464–471. (doi:10.1299/jsmeb.41.464)
22. Martynov SB, Mason DJ, Heikal MR. 2006 Numerical simulation of cavitation flows based on their hydrodynamic similarity. *Int. J. Eng. Res.* **7**, 283–296. (doi:10.1243/14680874JER04105)
23. Zhong W, He Z, Wang Q, Shao Z, Tao X. 2014 Experimental study of flow regime characteristics in diesel multi-hole nozzles with different structures and enlarged scales. *Int. Commun. Heat Mass Transfer* **59**, 1–10. (doi:10.1016/j.icheatmasstransfer.2014.10.001)
24. Payri R, Salvador FJ, Gimeno J, Venegas O. 2013 Study of cavitation phenomenon using different fuels in a transparent nozzle by hydraulic characterization and visualization. *Exp. Therm. Fluid Sci.* **44**, 235–244. (doi:10.1016/j.expthermflusci.2012.06.013)
25. Sou A, Hosokawa S, Tomiyama A. 2007 Effects of cavitation in a nozzle on liquid jet atomization. *Int. J. Heat Mass Transfer* **50**, 3575–3582. (doi:10.1016/j.ijheatmasstransfer.2006.12.033)
26. Sou A, Tomiyama A, Hosokawa A, Nigorikawa S, Maeda S. 2006 Cavitation in a two-dimensional nozzle and liquid jet atomization. *JSME Int. J. Ser. B* **49**, 1253–1259. (doi:10.1299/jsmeb.49.1253)
27. Mishra C, Peles Y. 2005 Cavitation in flow through a micro-orifice inside a silicon microchannel. *Phys. Fluids* **17**, 013601. (doi:10.1063/1.1827602)
28. Winklhofer E, Kull E, Kelz E, Morozov A. 2001 Comprehensive hydraulic and flow field documentation in mold throttle experiments under cavitation conditions. In *Proc. of the 17th ILASS-Europe Conference, Zurich, Switzerland, 2–6 September 2001*, pp. 574–579. Naples, Italy: Institute for Liquid Atomization and Spray Systems.
29. Oda T, Goda Y, Kanaike S, Aoki K, Ohsawa K. 2009 Experimental study about internal cavitating flow and primary atomization of a large-scaled VCO diesel injector with eccentric needle. In *Proc. 11th Triennial Int. Annu. Conf. on Liquid Atomization and Spray Systems (ICLASS), Vail, CO, 26–30 July 2009*, p. 132. Naples, Italy: Institute for Liquid Atomization and Spray Systems.

30. Ganippa LC, Bark G, Andersson S, Chomiak J. 2001 Comparison of cavitation phenomena in transparent scale-up single-hole diesel nozzles. In *Proc. of the 4th Int. Symp. on Cavitation, CAV2001, Pasadena, CA, 20–23 June 2001*. Pasadena, CA: California Institute of Technology.
31. Andriotis A, Arcoumanis C. 2009 Influence of vortex flow and cavitation on near nozzle diesel spray dispersion angle. *Atomization Sprays* **19**, 1–24. (doi:10.1615/AtomizSpr.v19.i3.30)
32. Mitroglou N, Gavaises M, Nouri JM, Arcoumanis C. 2011 Cavitation inside enlarged and real-size fully transparent injector nozzles and its effect on near nozzle spray formation. In *Proc. DIPSI Workshop 2011 on Droplet Impact Phenomena & Spray Investigation, Bergamo, Italy, 27 May, 2011*. See http://openaccess.city.ac.uk/1507/3/DIPSI_2011_Mitroglou.pdf.
33. Soteriou C, Andrews R, Smith M. 1995 Direct injection diesel sprays and the effect of cavitation and hydraulic flip atomization. SAE paper No. 950080.
34. Kim JH, Nishida K, Yoshizaki T, Hiroyasu H. 1997 Characterization of flows in the sac chamber and discharge hole of a DI diesel injection nozzle by using a transparent model nozzle. SAE paper no. 972942. SAE, Warrendale, PA, USA.
35. Arcoumanis C, Badami M, Flora H, Gavaises M. 2000 Cavitation in real-size multi-hole diesel injector nozzles. SAE paper no. 2000-01-1249. SAE, Warrendale, PA, USA.
36. Tullis JP. 1973 Cavitation scale effects for valves. *J. Hydraulics Div.* **99**, 1109–1128.
37. Chaves H, Knapp M, Kubitzek A, Obermeier F. 1995 Experimental study of cavitation in the nozzle hole of diesel injectors using transparent nozzles. SAE paper no. 950290. SAE, Warrendale, PA, USA.
38. Walther J, Schaller JK, Wirth R, Tropea C. 2000 Investigation of internal flow in transparent diesel injection nozzles using fluorescent particle image velocimetry (FPIV). In *Proc. 8th Int. Conf. on Liquid Atomization and Spray Systems, ICLASS, Pasadena, CA, 16–20 July 2000*. Pasadena, CA: California Institute of Technology.
39. Payri F, Payri R, Salvador FJ, Martínez-López J. 2012 A contribution to the understanding of cavitation effects in diesel injector nozzles through a combined experimental and computational investigation. *Comput. Fluids* **58**, 88–101. (doi:10.1016/j.compfluid.2012.01.005)
40. Lecoffre Y, Bonnin J. 1979 Cavitation tests and nucleation control. In *Proc. of the ASME Int. Symp. on Cavitation Inception, New York, NY, 2–7 December 1979*, pp. 141–145. New York, NY: American Society of Mechanical Engineers.
41. Arcoumanis C, Gavaises M, Flora H, Roth H. 2001 Visualization of cavitation in diesel engine injectors. *Mec. Ind.* **2**, 375–381. (doi:10.1016/S1296-2139(01)01119-8)
42. Lefebvre AH. 1989 *Atomization and sprays*. New York, NY: Taylor and Francis.
43. Nurick WH. 1976 Orifice cavitation and its effect on spray mixing. *J. Fluids Eng.* **98**, 681–689. (doi:10.1115/1.3448452)
44. Lichtarowicz A, Pierce ID. 1974 Cavitation and aeration effects in long orifices. In *Proc. of the Conf. on Cavitation, Edinburgh, UK, 3–5 September 1974*, pp. 129–144. London, UK: Institute of Mechanical Engineers.
45. Bergwerk W. 1959 Flow pattern in diesel nozzle spray holes. *Proc. Inst. Mech. Eng.* **170**, 655–660. (doi:10.1243/PIME_PROC_1959_173_054_02)
46. Lecoffre Y. 1999 *Cavitation: bubble trackers*. Rotterdam, The Netherlands: A.A. Balkema.
47. Blessing M, Konig G, Kruger C, Michels U, Schwarz V. 2003 Analysis of flow and cavitation phenomena in diesel injection nozzles and its effects on spray and mixture formation. SAE paper no. 2003-01-1358. SAE, Warrendale, PA, USA.
48. Benajes J, Pastor JV, Payri R, Plazas AH. 2004 Experiments for the different values of K-factor. *J. Fluids Eng.* **126**, 63. (doi:10.1115/1.1637636)
49. Badock C, Wirth R, Fath A, Leipertz A. 1999 Investigation of cavitation in real size diesel injection nozzles. *Int. J. Heat Fluid Flow* **20**, 538–544. (doi:10.1016/S0142-727X(99)00043-0)
50. Joseph D. 1995 Cavitation in a flowing liquid. *Phys. Rev. E* **51**, 1649–1650. (doi:10.1103/PhysRevE.51.R1649)
51. Martynov S. 2005 Numerical simulation of the cavitation process in diesel fuel injectors. PhD thesis, Brighton University, UK.
52. Decaix G, Goncalves E. 2013 Investigation of three dimensional effects on a cavitating Venturi flow. *Int. J. Heat Fluid Flow* **44**, 576–595. (doi:10.1016/j.ijheatfluidflow.2013.08.013)
53. Chen Y, Heister SD. 1996 Modelling hydrodynamic nonequilibrium in cavitating flows. *Trans. ASME J. Fluids Eng.* **118**, 172–178. (doi:10.1115/1.2817497)

54. Stanley C, Barber T, Rosengarten G. 2014 Re-entrant jet mechanism for periodic cavitation shedding in a cylindrical orifice. *Int. J. Heat Fluid Flow* **50**, 169–176. (doi:10.1016/j.ijheatfluidflow.2014.07.004)
55. Franc JP. 2001 Partial cavity instabilities and re-entrant jet. In *Proc. of the 4th Int. Symp. on Cavitation, CAV2001, Pasadena, CA, 20–23 June 2001*. Pasadena, CA: California Institute of Technology.
56. Knapp RT, Daily JW, Hammitt FG. 1970 *Cavitation*. New York, NY: McGraw-Hill.
57. Dumont N, Simonin O, Habchi C. 2000 Cavitating flow in diesel injectors and atomisation: a bibliographical review. In *Proc. of the 17th ILASS-Europe Conference, Zurich, Switzerland, 2–6 September 2001*. Naples, Italy: Institute for Liquid Atomization and Spray Systems.
58. Sato K, Saito Y. 2001 Unstable cavitation behaviour in circular-cylindrical orifice flow. In *Proc. of the 4th Int. Symp. on Cavitation, CAV2001, Pasadena, CA, 20–23 June 2001*. Pasadena, CA: California Institute of Technology.
59. Callenaere M, Franc JP. 2001 The cavitation instability induced by the development of a re-entrant jet. *J. Fluid Mech.* **444**, 223–256. (doi:10.1017/S0022112001005420)
60. Ganesh H, Makiharju SA, Ceccio SL. 2016 Bubbly shock propagation as a mechanism for sheet-to-cloud transition of partial cavities. *J. Fluid Mech.* **802**, 37–78. (doi:10.1017/jfm.2016.425)
61. Gnanaskandan A, Mahesh K. 2016 Large eddy simulation of the transition from sheet to cloud cavitation. *Int. J. Multiphase Flow* **83**, 86–102. (doi:10.1016/j.ijmultiphaseflow.2016.03.015)
62. Ferrari A, Rapetto N. 2017 A contribution to the understanding of physics and dynamics of hydrodynamic cavitation. In *Proc. 2017 ASME Fluids Engineering Division Summer Meeting, FEDSM2017, Waikoloa, HI, 30 July–4 August 2017*.
63. Von Kuensberg Sarre C, Kong SC, Reitz RD. 1999 Modeling the effects of injector nozzle geometry on diesel sprays. SAE paper no. 1999-01-0912. SAE, Warrendale, PA, USA.
64. Sou A, Bicer B, Tomiyama A. 2014 Numerical simulation of incipient cavitation flow in a nozzle of a fuel injector. *Computer Fluids* **103**, 42–48. (doi:10.1016/j.compfluid.2014.07.011)
65. He Z, Tao X, Zhong W, Leng X, Wang Q, Zhao P. 2015 Experimental and numerical study of cavitation inception phenomenon in diesel injector nozzles. *Int. Commun. Heat Mass Transfer* **65**, 117–124. (doi:10.1016/j.icheatmasstransfer.2015.04.009)
66. Fox TA, Stark J. 1989 Discharge coefficients for miniature fuel injectors. *Proc. Inst. Mech. Eng. G J. Aerosp. Eng.* **203**, 75–78. (doi:10.1243/PIME_PROC_1989_203_056_01)
67. Laoonual Y, Yule AJ, Walmsley SJ. 2001 Internal fluid flow and spray visualization for a large-scale VCO orifice injector nozzle. In *Proc. of the 17th ILASS-Europe Conference, Zurich, Switzerland, 2–6 September 2001*. Naples, Italy: Institute for Liquid Atomization and Spray Systems.
68. Merrit HE. 1967 *Hydraulic control systems*. New York, NY: John Wiley & Sons.
69. Cioncolini A, Scenini F, Duff J, Szolcek M, Curioni M. 2016 Choked cavitation in micro-orifices: an experimental study. *Exp. Therm. Fluid Sci.* **74**, 49–57. (doi:10.1016/j.expthermflusci.2015.12.004)
70. Lichtarowicz A, Duggins RK, Markland E. 1965 Discharge coefficients for incompressible non-cavitating flow through long orifices. *J. Mech. Eng. Sci.* **7**, 210–219. (doi:10.1243/JMES_JOUR_1965_007_029_02)
71. Yu B, Fu PF, Zhang T, Zhou H-C. 2013 The influence of back pressure on the flow discharge coefficients of plain orifice nozzle. *Int. J. Heat Fluid Flow* **44**, 509–514. (doi:10.1016/j.ijheatfluidflow.2013.08.005)
72. Chisholm D. 1983 *Two-phase flow in pipelines and heat exchangers*. London, UK: Godwin.
73. Lamb H. 1997 *Hydrodynamics*. Cambridge, UK: Cambridge University Press.
74. Viersma TJ. 1962 Designing load-compensated fast response hydraulic servos. *Control Eng.* **50**, 111–114.
75. Rouse H, Abul-Fetouh A. 1950 Characteristics of irrotational flows through axially symmetric orifices. *J. Appl. Mech.* **17**, 421–426.
76. Goncalves E, Charriere B. 2014 Modelling for isothermal cavitation with a four-equation model. *Int. J. Multiphase Flow* **59**, 54–72. (doi:10.1016/j.ijmultiphaseflow.2013.10.015)
77. Kubota A, Kato H, Yamaguchi H. 1992 A new modelling of cavitating flows: a numerical study of unsteady cavitation on a hydrofoil section. *J. Fluid Mech.* **254**, 151–181. (doi:10.1017/s002211209200003x)

78. Bicer B, Sou A. 2016 Application of the improved cavitation model to turbulent cavitating flow in fuel injector nozzle. *Appl. Math. Modell.* **40**, 4712–4726. (doi:10.1016/j.apm.2015.11.049)
79. Ishii C, Hibiki T. 2006 *Thermo-fluid dynamics of two-phase flow*. Berlin, Germany: Springer.
80. Hoang H, Galliero G. 2016 Predictive Tait equation for non-polar and weakly polar fluids: applications to liquids and liquid mixtures. *Fluid Phase Equilib.* **425**, 143–151. (doi:10.1016/j.fluid.2016.05.026)
81. Neece GA, Squire DR. 1968 On the Tait and related empirical equations of state. *J. Phys. Chem.* **72**, 128–136. (doi:10.1021/j100847a024)
82. Salvador FJ, Romero JV, Roselló MD, Martínez-López J. 2010 Validation of a code for modeling cavitation phenomena in diesel injector nozzles. *Math. Comput. Modell.* **52**, 1123–1132. (doi:10.1016/j.mcm.2010.02.027)
83. Saurel R, Petitpas F, Berry RA. 2009 Simple and efficient relaxation methods for interfaces separating compressible fluids, cavitating flows and shocks in multiphase mixtures. *J. Comput. Phys.* **228**, 1678–1712. (doi:10.1016/j.jcp.2008.11.002)
84. Beck M, Iben U, Mittwollen N, Iben HK, Munz CD. 2001 On solution of conservation equations in cavitated hydraulic pipelines. In *Proc. 3rd Int. Symp. on Computational Technologies for Fluid, Thermal and Chemical Systems with Industrial Applications, Atlanta, GA, 22–26 July 2001*. New York, NY: American Society of Mechanical Engineers.
85. Ferrari A, Mittica A, Manno M. 2008 Cavitation analogy to gasdynamic shocks: model conservativeness effects on the simulation of transient flows in high-pressure pipelines. *ASME Trans. J. Fluids Eng.* **130**, 0.313041. (doi:10.1115/1.2842226)
86. Bejan A. 2006 *Advanced engineering thermodynamics*. New York, NY: John Wiley & Sons.
87. Goncalves E, Patella RF. 2009 Numerical simulation of cavitating flows with homogeneous models. *Comput. Fluids* **38**, 1682–1696. (doi:10.1016/j.compfluid.2009.03.001)
88. Hejranfar K, Ezzatneshan E, Fattah-Hesari K. 2015 A comparative study of two cavitation modeling strategies for simulation of inviscid cavitating flows. *Ocean Eng.* **108**, 257–275. (doi:10.1016/j.oceaneng.2015.07.016)
89. Senocak I, Shyy W. 2002 Evaluation of cavitation models for Navier-Stokes computations. In *Proc. of the 2002 ASME Fluids Engineering Division Summer Meeting, Montreal, Canada, 14–18 June 2002*, pp. 395–401. New York, NY: American Society of Mechanical Engineers.
90. Merkle CL, Feng JZ, Buelow PEO. 1998 Computational modeling of the dynamics of sheet cavitation. In *Proc. of the 3rd Int. Symp. on Cavitation, Grenoble, France, 7–10 April 1998* (eds JM MIchel, H Kato), pp. 307–311. Grenoble, France: Université Joseph Fourier.
91. Kunz RF, Boger DA, Chyczewski TS, Stinebring DR, Gibeling HJ. 1999 Multi-phase CFD analysis of natural and ventilated cavitation about submerged bodies. In *Proc. of the 3rd ASME/JSME Joint Fluids Engineering Conference* (*FEDSM '99*), *San Francisco, CA, 18–23 July 1999*. New York, NY: American Society of Mechanical Engineers.
92. Kunz RF, Boger DA, Chyczewski TS, Stinebring DR, Lindau JW, Gibeling HJ, Venkateswaran S, Govindan TR. 2000 A preconditioned Navier-Stokes method for two-phase flows with application to cavitation prediction. *Comput. Fluids* **29**, 849–875. (doi:10.1016/S0045-7930(99)00039-0)
93. Ahuja V, Hosangadi A, Arunajatesan S. 2001 Simulations of cavitating flows using hybrid unstructured meshes. *J. Fluids Eng.* **123**, 331–339. (doi:10.1115/1.1362671)
94. Senocak I, Shyy W. 2004 Interfacial dynamics-based modelling of turbulent cavitating flows. Part I: model development and steady-state computations. *Int. J. Numer. Methods Fluids* **44**, 975–995. (doi:10.1002/fld.692)
95. Yuan W, Sauer J, Schnerr GH. 2001 Modeling and computation of unsteady cavitation flows in injection nozzles. *Mec. Ind.* **2**, 383–394. (doi:10.1016/S1296-2139(01)01120-4)
96. Fujimoto H, Mishikori T, Tsumakoto T, Senda J. 1994 Modeling of atomization and vaporization process in flash boiling spray. In *Proc. of the 6th Inter. Conf. on Liquid Atomization and Spray Systems* (*ICLASS 94*), *Rouen, France, 18–22 July 1994*, paper No. VI-13. Danbury, CT: Begell House.
97. Alajbegovic A, Meister G, Greif D, Basara B. 2002 Three phase cavitating flows in high-pressure swirl injectors. *Exp. Therm. Fluid Sci.* **26**, 677–681. (doi:10.1016/S0894-1777(02)00179-6)
98. Alajbegovic A, Grogger HA, Philipp H. 1999 Calculation of transient cavitation in nozzle using the two-fluid model. In *Proc. 12th ILASS-Americas Annual Conf., Indianapolis, IN, 17–19 May 1999*, pp. 373–377.

99. Fourest T, Laurens JM, Deletombe E, Dupas J, Arrigoni M. 2014 Analysis of bubble dynamics created by hydrodynamic ram in confined geometries using the Rayleigh-Plesset equation. *Int. J. Impact Eng.* **73**, 66–74. (doi:10.1016/j.ijimpeng.2014.05.008)
100. Chahine GL. 2004 Nuclei effects on cavitation inception and noise. In *Proc. 25th Symp. on Naval Hydrodynamics, St. Johns, Newfoundland and Labrador, Canada, 8–13 August 2004*. Washington, DC: National Academies Press.
101. Giannadakis E, Gavaises M, Roth H, Arcoumanis C. 2004 Cavitation modelling in single-hole injector based on Eulerian-Lagrangian approach. In *Proc. THIESEL 2004 8th Conf. on Thermo- and Fluid Dynamic Processes in Diesel Engines, Valencia, Spain, 9–12 September 2004*. Valencia, Spain: Universidad Politecnica de Valencia.
102. Schrage RW. 1953 *A theoretical study of interphase mass transfer*. New York, NY: Columbia University Press.
103. Akhatov I, Lindau O, Topolnikov A, Mettin R, Vakhitova N, Lauterborn W. 2001 Collapse and rebound of a laser-induced cavitation bubble. *Phys. Fluids* **13**, 2805–2819. (doi:10.1063/1.1401810)
104. Fujikawa S, Akamatsu T. 1980 Effects of the non-equilibrium condensation of vapor on the pressure wave produced by the collapse of a bubble in a liquid. *J. Fluid Mech.* **97**, 481–516. (doi:10.1017/S0022112080002662)
105. Iben U, Wrona F, Munz CD, Beck M. 2002 Cavitation in hydraulic tools based on thermodynamic properties of liquid and gas. *ASME J. Fluids Eng.* **124**, 1011–1017. (doi:10.1115/1.1514200)
106. Keller JB, Kolodner II. 1956 Damping of underwater explosions bubble oscillations. *J. Appl. Phys.* **27**, 1152–1161. (doi:10.1063/1.1722221)
107. Hegedus F, Koch S, Garen W, Pandula Z, Paál G, Kullmann L, Teubner U. 2013 The effect of high viscosity on compressible and uncompressible Rayleigh-Plesset type bubble models. *Int. J. Heat Fluid Flow* **42**, 200–208. (doi:10.1016/j.ijheatfluidflow.2013.04.004)
108. Harkin A, Nadim A, Kaper TJ. 1999 On acoustic cavitation of slightly subcritical bubbles. *Phys. Fluids* **2**, 274–287. (doi:10.1063/1.869878)
109. Oba R, Ikohagi T, Sato K, Ito Y, Miyakura H. 1986 Stochastic behavior (randomness) of desinent cavitation. *ASME Trans. J. Fluids Eng.* **108**, 438. (doi:10.1115/1.3242601)
110. Sato K, Kakutani K. 1994 Measurements of cavitation inception. *JSME Int. J. Ser. B* **37**, 306–312. (doi:10.1299/jsmeb.37.306)
111. Plesset MS. 1949 The dynamics of cavitation bubbles. *ASME J. Appl. Phys.* **16**, 228–231.
112. Liu Z, Brennen CE. 1998 Cavitation nuclei population and event rates. *Trans. ASME J. Fluid. Eng.* **120**, 728–737. (doi:10.1115/1.2820730)
113. Wang G *et al.* 2001 Dynamics of attached turbulent cavitating flows. *Progr. Aerospace Sci.* **37**, 551–581. (doi:10.1016/S0376-0421(01)00014-8)
114. Rood EP. 1991 Review—mechanism of cavitation inception. *Trans. ASME J. Fluids Eng.* **113**, 163–175. (doi:10.1115/1.2909476)
115. ITTC. 1993 Report of Cavitation Committee. In *Proc. 20th Int. Towing Tank Conf., San Francisco, CA, 19–25 September 1993*. See http://ittc.info/media/2372/report-of-the-cavitation-committee.pdf.
116. Henry P. 1978 Influence of the amount of bubble nuclei on cavitation tests of Francine turbine. In *Proc. of the ASME Symp. Cavitation and Polyphase Flow Forum, Fort Collins, CO, 12–14 June 1978*, pp. 23–28. New York, NY: American Society of Mechanical Engineers.
117. Billet ML. 1985 Cavitation nuclei measurements—a review. In *Proc. of the ASME Cavitation and Multiphase Flow Forum, Albuquerque, NM, 24–26 June 1985*. New York, NY: American Society of Mechanical Engineers.
118. Arndt REA, Ippen AT. 1968 Rough surface effects on cavitation inception. *ASME J. Basic Eng.* **90**, 249–261. (doi:10.1115/1.3605086)
119. Payri R, Salvador FJ, Gimeno J, de la Morena J. 2009 Study of cavitation phenomena based on a technique for visualizing bubbles in a liquid pressurized chamber. *Int. J. Heat Fluid Flow* **30**, 768–777. (doi:10.1016/j.ijheatfluidflow.2009.03.011)
120. Mishra C, Peles Y. 2005 Size scale effects on cavitating flows thorugh micro-orifices entrenched in rectangular microchannels. *J. Microelectromech. Syst.* **14**, 987–998. (doi:10.1109/JMEMS.2005.851800)
121. Tullis P. 1971 Choking and supercavitating valves. *J. Hydraulics Div.* **97**, 1931–1945.
122. Bernad SI, Resiga RS. 2012 Numerical model for cavitational flow in hydraulic poppet valves. *Modell. Simul. Eng.* **2012**, 742162. (doi:10.1155/2012/742162)